Original Research Article

International journal of spray and combustion dynamics

International Journal of Spray and Combustion Dynamics
2018, Vol. 10(3) 185–210

DOI: 10.1177/1756827718763559
journals.sagepub.com/home/scd

SAGE

Measurements in swirling spray flames at blow-off

Ruoyang Yuan[1], James Kariuki[2] and Epaminondas Mastorakos[3]

Abstract

Various characteristics of swirling spray flames of ethanol, n-heptane, n-decane, and n-dodecane have been measured at conditions far from and close to blow-off using phase Doppler anemometry and OH* chemiluminescence, OH-planar laser-induced fluorescence, and Mie scattering at 5 kHz. The blow-off transient has also been examined. The OH* showed that the two main heat release regions lie around the spray jet at the inner recirculation zone and along the outer shear layer between the inner recirculation zone and the annular air jet. The heat release region is shortened and more attached as the flame approached blow-off. Mie images and phase Doppler anemometry data showed a wider dispersion of the ethanol spray compared to the other fuels. Similar spatial distributions of the Sauter mean diameter were observed for the four fuels for identical flow conditions, with the Sauter mean diameter value increasing with decreasing fuel volatility, but with the exception of significant presence of droplets in the nominally hollow cone for the ethanol spray. The OH-planar laser-induced fluorescence measurements showed an intermittent lift-off from the corner of the bluff body and the average lift-off height decreased with increasing air velocity, with less extinction along the inner flame branch especially for the heavier fuels. At the blow-off conditions, local extinctions appeared at both flame branches. The blow-off process followed a gradual reduction of the size of the flame, with the less volatile fuels showing a more severe flame area reduction compared to the condition far from blow-off. The average blow-off duration, τ_{ext}, calculated from the evolution of the area-integrated OH* signal, was a few tens of milliseconds and for all conditions investigated the ratio $\tau_{ext}/(D/U_B)$ was around 11, but with large scatter. The measurements provide useful information for validation of combustion models focusing on local and global extinction.

Keywords

Spray flame, swirl, extinction, blow-off

Date received: 2 November 2016; accepted: 15 February 2018

1. Introduction

Lean combustion has the promise of significantly reducing NOx emissions, but the accompanying increased danger of global extinction, referred to here as blow-off, needs to be addressed. Lean blow-off (LBO) limits play an important role in establishing the combustor operating envelope. From an engineering perspective, experimental investigations focusing on establishing a model to correlate LBO limits of spray flames for various burner geometries and operating conditions have been carried out.[1–6] Whereas the effect of volatility of multi-component fuels on flame blow-off has been investigated extensively,[1] the effect of volatility of single-component fuels for identical flow and burner conditions has received less attention. Additionally, little information is available on the structure of spray flames at conditions near blow-off, which can help not only with designing combustors with better stability limits, but also promote our fundamental understanding of a challenging phenomenon affected by a range of factors including turbulence, kinetics, and phase change. Although the structure of swirl spray flames

[1]Loughborough University, Loughborough, UK
[2]Bristol University, Bristol, UK
[3]Engineering Department, Hopkinson Laboratory, University of Cambridge, Cambridge, UK

Corresponding author:
Epaminondas Mastorakos, Engineering Department, Hopkinson Laboratory, University of Cambridge, Cambridge CB2 1PZ, UK.
Email: em257@eng.cam.ac.uk

has been studied from the perspective of droplet velocities and global stability,[7,8] further work is needed to extend such data to conditions very close to blow-off.

Local flame extinction is a phenomenon observed at conditions close to LBO,[6] but the mechanism linking local and global extinction is not always clear. In non-premixed gaseous fuel flames, local extinction has been studied extensively and a solid body of knowledge exists concerning the degree and causes of local extinction, from both experimental[9–25] and numerical[26–38] viewpoints. Typically, local extinction is suggested to result from high scalar dissipation rates. In piloted jets, where the majority of our current knowledge is based on, the degree of local extinction has been measured[21–25] and this has provided a very challenging dataset for model validation. In swirling non-premixed flames, additional characteristics are observed such as local extinction occurring also at conditions far from blow-off,[5,10,11] and the occurrence of local extinctions strongly correlating with high shear stress regions which are found to not necessarily overlap with the mean stoichiometric contours.[10] For either piloted jet or swirl flames of gaseous fuels, capturing the exact blow-off limit by a combustion CFD calculation still seems beyond our capabilities.

Only a few studies have investigated local extinctions in turbulent swirling spray flames. Local break-ups along the flame sheet were observed in swirling spray flames of heptane[5] using 5 kHz OH-planar laser-induced fluorescence (PLIF). Following this study, simultaneously acquired CH_2O- and OH-PLIF measurements were obtained for a heptane spray flame[39] to estimate heat release (HR) rates using the burner that is used in this paper. The results show that the flames studied take a predominantly non-premixed character, with the OH signal corresponding well to the HR regions represented by the overlaps of CH_2O and OH radicals. Interestingly, the outline of the CH_2O signals approximates the stoichiometric mixture fraction (ξ_{st}) iso-line, as inferred from laminar flame calculations,[39,40] and this is further explored in this paper to provide a measure of local extinction.

Local extinction behaviour has also been found to depend on the fuel vapour pressure of pilot-stabilised jet flames of dilute sprays of acetone or ethanol approaching global extinction.[41] Close to blow-off, an absence of local extinctions was observed in acetone flames where the OH regions were continuous, while possible local extinction was indicated in ethanol flames where the OH signal was separated. Thus, the different vapour pressure of the fuels is suggested to add complexity to the mixing and reaction fields and requires further study.

The global extinction condition and mechanism has been investigated in turbulent gaseous flames (premixed[42–51] and non-premixed[5,52–55]), in laminar spray flame simulations,[56–59] and in counterflow configurations experimentally.[60] In premixed flames, global blow-off is found to be preceded by the increasing occurrence of local extinction events along the flame sheet as observed in rod-stabilised premixed flames[43] and bluff body-stabilised flames.[46–51] In particular, the dominant location of extinction is not at the anchoring point, but further downstream where the Karlovitz number is higher[50] and this leads to the accumulation of unburnt gases entering the recirculation zone from the downstream side and to the detection of partial combustion species like CH_2O.[51]

For non-premixed flames, global blow-off is suggested to occur at a flow condition where the characteristic mixing time between entrained hot combustion gases and unburned jet fluid is small relative to a combustion timescale.[53] The transient process of methane–air jet flame blow-off revealed that the prior disappearance of the axially oriented trailing diffusion flame branch acts as a predictor of blow-off. Blow-off then occurred when the leading edge progressing downstream reached the vicinity of the lean-limit contour.[61]

In swirling non-premixed flames, the addition of swirl is found to improve the blow-off limits.[10,62] The transient process of the blow-off event in a confined swirling non-premixed flame was first visualised by fast imaging (5 kHz) of OH* in Cavaliere et al.,[5] which indicated the shortening and fragmentation of the flame brush during the blow-off event. It is also worth noting that recent efforts for both premixed and non-premixed flames with fast OH* have quantified the duration of the blow-off event one order of magnitude larger compared to a characteristic residence time in the combustor.[5,49,50]

Very limited information exists on the behaviour of swirling spray flames during the blow-off event.[5,63] Cavaliere et al.[5] compared heptane spray flames with methane premixed and methane non-premixed flames in the same swirl burner at conditions both close to and during the blow-off event. Significant changes in the spray flame shape were observed, where the flame was more attached to the bluff body at conditions closer to blow-off. The duration of the blow-off event for all flames investigated was of the order of tens of milliseconds, with a faster extinction process observed for the spray flame compared to the gaseous flames.[5] This spray flame has also been studied using large Eddy simulations (LESs) combined with the conditional moment closure[63] combustion model. The simulations successfully captured local extinction and global blow-off phenomena observed in the experiments in Cavaliere et al.[5]

Further work is necessary both for the quantification of local extinction and global blow-off transient, and

for characterising spray flames at conditions close to blow-off. Information on flames at such conditions can be very productive for validating turbulent combustion models. In the present paper, the work in Cavaliere et al.[5] and Yuan et al.[39] with heptane was continued and new experiments in the same swirl burner were performed including more volatile (ethanol) and less volatile (n-decane, n-dodecane) fuels to examine any fuel volatility effect on blow-off limits and on flame structure from the perspective of local extinctions. The main objectives of this work are to investigate the effect of fuel properties on the behaviour of swirling spray flames at both stable and blow-off conditions, to develop further understanding of the role of local flame extinctions in the global extinction of recirculating spray flames, and to provide various metrics of extinction for validating combustion models.

2. Methods

2.1 Apparatus

A bluff body swirl spray burner was used to study flames at different conditions, focused on local extinctions and blow-off. The same burner was studied before by Cavaliere et al.[5] for blow-off studies of methane premixed and non-premixed and heptane spray flames, and (with a different enclosure) by Marchione et al.[64] for ignition of heptane spray flames. An important difference is a new atomiser adopted in this work to perform experiments with a wider fuel flow rate range and various liquid fuels. A schematic of the burner is shown in Figure 1. A pressurised axial-flow hollow cone atomiser (Lechler, Part#.212.054.17.AC) was fitted into a conical bluff body holder. The bore diameter of the atomiser nozzle is 0.2 mm, while the narrowest exit diameter is 0.15 mm. The spray angle is 60° (nominal; manufacturer's data). The bluff body diameter is 25 mm (Figure 1). The air stream passed through an annular swirler before entering the combustion chamber, which is enclosed to the sides by four Quartz pieces of 97×150 mm (Figure 1). The swirler has a constant vane angle of 60° and a swirl number of 1.23 calculated by the expression in Beér and Chigier.[65] The burner has also been used for exploring the simultaneous CH_2O–OH PLIF technique for heptane by Yuan et al.,[39] while the present work focuses on a comparison between different fuels and on the use of fast diagnostics suitable for studying the blow-off transient as well as the steady-state flame. The dataset of Yuan et al.[39] is re-analysed here (Section 3.6) to provide a new metric quantifying local extinction to supplement the quantification offered by the fast OH-PLIF system discussed in Section 2.3.

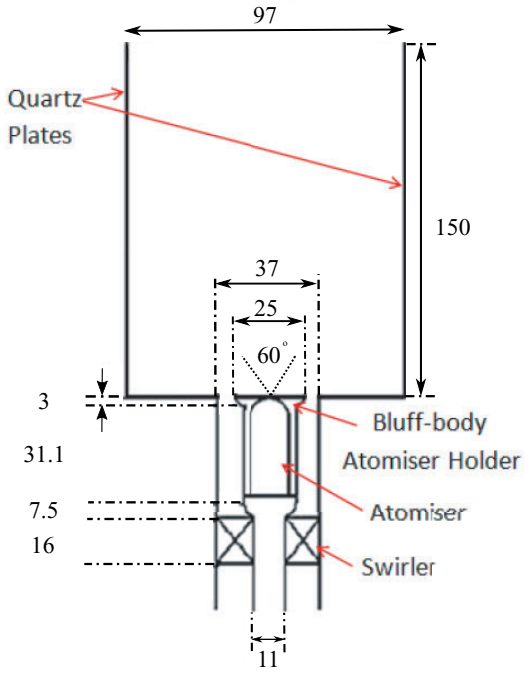

Figure 1. Schematic of the bluff body swirl spray burner. All dimensions in millimetre.

2.2 Flow conditions

The liquid fuel was pressurised by nitrogen (BOC, 99.9995% vol/vol purity) supplied from a compressed cylinder regulated at 0–6.0 bar. The liquid flow rate was altered by adjusting the set pressure from the fuel tank and was monitored by a liquid mass flow controller (MFC) (Bronkhorst, LIQUI-flow, L30, 0–2 g/s, uncertainty of ±0.02 g/s). The fuels used in this work were ethanol, n-heptane, n-decane, and n-dodecane. The fuel flow rate range was in the range of 0.15–0.45 g/s. The calibration of the MFC was performed by measuring the weight (±0.1 g) of the liquid output and timing with a hand-held stopwatch (±0.01 s, user error 0.1 s) as a function of the reading on the MFC for each fuel.

The air was supplied by the laboratory compressor, filtered for water, particulates, and oil content. The air flow rate was controlled by an MFC (Alicat, MFC 1000 SLPM, uncertainty of ± (0.8% of reading + 0.2% of full scale (FS)); repeatability of ± 0.2% of FS). The operating flow range was 500–990 SLPM, which corresponded to a bulk velocity between 14.3 and 28.2 m/s.

The flow conditions investigated are summarised in Table 1. Codes 'S' imply stable flames, while codes 'B' imply flames at the blow-off velocity. For all these flames, the fuel mass flow rate was 0.27 g/s, but some experiments were also done at different fuel flow rates.

Various non-dimensional parameters, given in Table 2 and Table 3, are calculated as follows

$$Re_l = \frac{U_l D_l}{\nu_l}, \quad Re_g = \frac{U_b D}{\nu_g}, \; We_l = \frac{\rho_l U_l^2 D_l}{\sigma_l}$$
$$We_g = \frac{\rho_g U_l^2 D_l}{\sigma_l}, \quad Ta = \frac{\rho_l}{\rho_g}\left(\frac{Re_l}{We_l}\right)^2, \quad Oh = \frac{\sqrt{We_l}}{Re_l} \tag{1}$$

where U_l is the liquid jet velocity at the nozzle exit; U_b is the air bulk velocity at the annulus; D_l is the nozzle diameter at its exit; D is the bluff body diameter; ν_l and ν_g are the kinematic viscosity of liquid and gas, respectively; σ_l is the liquid surface tension coefficient; and ρ_l and ρ_g are liquid and gas density, respectively. The physical properties of the fuels and air were evaluated at 20°C. The local Weber number is useful when considering the possibility of droplet break-ups. Since its value varies from location to location, the Weber number and other non-dimensional parameters listed in equation (1) are examined at the fuel jet exit as a reference. As the air velocity is relatively small compared to the liquid jet velocity at the exit, the relative velocity in the equation of We_l is taken as the liquid jet velocity (U_l).

Table 1. Conditions used for most of the experiments, corresponding to various stable and blow-off conditions. For all, the fuel mass flow rate was 0.27 g/s. U_b corresponds to the bulk air velocity at the annular opening around the bluff body.

Fuel type	Name	Case	U_b (m/s)	$\phi_{overall}$
Ethanol	E1S1	Stable	17.1	0.19
	E1S2	Stable	20	0.16
	E1B	Blow-off	21.6	0.15
n-Heptane	H1S1	Stable	17.1	0.32
	H1S2	Stable	20	0.27
	H1B	Blow-off	22.8	0.24
n-Decane	D1S1	Stable	17.1	0.31
	D1S2	Stable	20	0.27
	D1B	Blow-off	20.3	0.27
n-Dodecane	DD1S1	Stable	14.3	0.38
	DD1S2	Stable	17.1	0.32
	DD1B	Blow-off	20.1	0.27

2.3 Diagnostics

2.3.1 Phase Doppler anemometry

Droplet size and velocity distributions were measured using standard two-channel laser Doppler/phase Doppler anemometry (LDA/PDA, DANTEC). One channel was used to measure the axial velocity component as well as droplet diameter while the other channel measured the radial velocity component simultaneously. Acquisition at each measurement location was limited to a 30 s duration and a maximum collection of 20,000 samples. The validation rate for the Doppler burst was close to 100% and the spherical validation was over 80% during the acquisition for all locations. The present instrument and its controlling software operated only within a user-supplied diameter range and this was set at 0–100 μm, which may underestimate the Sauter mean diameter (SMD) values in locations with large droplets. The measurement uncertainties of the mean values (MVs) of the axial, radial velocity, and

Table 2. Fuel properties (evaluated at 20°C) and flow parameters at the main test conditions.

Name	E1S1	E1S2	H1S1	H1S2	D1S1	D1S2	DD1S1	DD1S2
U_b (m/s)	17.11	19.97	17.11	19.97	17.11	19.97	14.26	17.11
U_l (m/s)	10.68	10.68	12.64	12.64	11.93	11.93	11.41	11.41
ρ_l (kg/m^3)	804.9		668.3		720.7		753.2	
σ (N/m)	2.21×10^{-2}		2.01×10^{-2}		2.38×10^{-2}		2.54×10^{-2}	
ν_l (m^2/s)	1.42×10^{-6}		0.61×10^{-6}		1.29×10^{-6}		1.98×10^{-6}	
p_{vap} (kPa)	5.65		4.70		0.12		0.01	
ΔH_{vap} (kJ/kg)	938.2		360.5		352.5		339.3	
P (kW)	8.0		12.0		11.94		11.92	
Re_l	1504		4192		1849		1153	
Re_g	13,466	15,711	13,466	15,711	13,466	15,711	11,222	13,466
We_l	830		1098		860		774	
We_g	1.23		1.95		1.42		1.22	
Ta	2220		8201		2800		1406	
Oh	0.019		0.008		0.016		0.024	

Table 3. Flow parameters of the stable ethanol flames used in OH* measurements to explore fuel flow rate effects.

Name	E0S0	E1S0	E4S1	E5S1
$\dot{m}_f$ (g/s)	0.20	0.27	0.40	0.45
U_b (m/s)	14.3	14.3	17.1	17.1
U_l (m/s)	7.9	10.7	15.8	17.8
ρ_l (kg/m^3)	804.9			
σ (N/m)	2.21×10^{-2}			
ν_l (m^2/s)	1.42×10^{-6}			
Re_l	1114	1504	2228	2506
Re_g	11,222		13,466	
We_l	456	830	1823	2307
We_g	0.7	1.2	2.7	3.4
Ta	4046	2220	1011	800
Oh	0.019			
P (kW)	6	8	12	13

the size are 0.3, 0.1, and 0.2%, respectively, at the spray jet locations, and are 5, 3, and 3% at the farthest radius locations where the smallest number of data points was obtained.

2.3.2 Chemiluminescence. OH* chemiluminescence was measured as an indicator of HR both at stable conditions and during the blow-off event. An IRO intensifier (LaVision, spectral range of 190–800 nm) was fitted with a UV filter (270–370 nm) for OH*. The intensifier was coupled with a Photon SA1.1 monochrome high-speed CMOS camera with 1024 × 1024 pixel resolution. OH* chemiluminescence was captured at 5 kHz. About 1000–5000 images (0.2–1.0 s) were recorded per run. The obtained image series were averaged and then the inverse Abel Transform was applied to obtain a mean 2D HR image. For the blow-off cases, the time series was recorded and the blow-off event duration was calculated by the duration of integral OH* intensity drop from 90 to 10% of its MV, following Kariuki et al.[50] and Cavaliere et al.[5] Chemiluminescence is used here in a qualitative sense in order to determine the flame shape and location, rather than as a quantitative measure of HR because the present flames are not fully premixed.

2.3.3 PLIF. OH-PLIF was used to visualise the flame sheet. The diagnostic system was used previously in Cavaliere et al.[5] and Kariuki et al.[50] The OH-PLIF system consisted of a high-repetition rate diode solid state laser (532 nm, model JDSU Q201-HD), with a power of 14 W at 5 kHz and a pulse length of around 18 ns, and a SIRAH Credo high-speed dye laser (model 2400), with the output beam at 566 nm doubled by a BBO crystal. The output beam was tuned near 283 nm to excite the Q1 (6) line in the A1Σ–X2Π(1,0) band. The output power was 300 mW at 5 kHz (60 μJ/pulse). The laser beam was expanded into a sheet of around 0.23 mm thick and 35 mm high using sheet optics. An IRO intensifier (LaVision, spectral range of 190–800 nm) was fitted with a narrower filter (300–325 nm) for OH-PLIF compared to OH*. The intensifier was coupled with the Photron SA1.1 monochrome high-speed CMOS camera with 1024 × 1024 pixel resolution. The OH-PLIF movies were captured at 5 kHz. About 1000–5000 images (0.2–1.0 s) were recorded per run. The OH fluorescence signal is not examined in a quantitative sense, but only as a qualitative indicator of the presence or not of OH.

2.3.4 Mie scattering. The 2D Mie scattering from the spray droplets was also measured with 532 nm wavelength incident laser light and a narrow band laser line filter. The laser sheet thickness was around 1 mm. The pulse laser and camera systems are the same as described above for the OH-PLIF measurement. A neutral density filter was fitted before the camera to prevent damage to the camera. A sequence of 1000 images of stable flames and 800 images of unstable flames before the blow-off transient was averaged to get the mean Mie scattering profiles so as to visualise the spray location. As for OH-PLIF, the usefulness of the Mie scattering is of a qualitative nature and to guide the selection of initial conditions for the spray in numerical simulations.

2.4 Blow-off condition determination

In order to reach the LBO limit of the spray flame, the fuel flow rate was kept fixed and the air flow rate was gradually increased in steps of approximately 2% (0.258 m/s) every 40–60 s until blow-off occurred recording the blow-off velocity, U_B. At each fuel flow rate, an average blow-off velocity from at least 10 individual measurements was calculated. This average blow-off velocity is included in Table 1 for E1B, H1B, D1B, and DD1B and plotted later as a function of fuel flow rate for all fuels.

For some experiments, the blow-off event was recorded and was used to determine the duration of the transient. From such records, and using only the portions before the blow-off event begun, the flame characteristics of the flame at nominally the blow-off condition were determined so as to compare with the statistically steady behaviour at conditions far from blow-off.

2.5 Data processing

The inverse Abel transform was applied to the mean images of the line-of-sight OH* data to obtain local HR

images. There was asymmetry in the average 2D projected image due to a slight burner non-uniformity. A reconstructed axisymmetric image from the selected half of the mean image was used for the inverse Abel inversion. The inversion has a drawback in producing artificial structures on the central axis ($r = 0$).

The OH-PLIF images were filtered using a 2D median non-linear filter for noise reduction (3×3 filter size) and corrected for inhomogeneities in the laser sheet profile for further processing to get various quantities such as morphological features of isolated OH regions and the lift-off height of the flame from the bluff body. The laser sheet profile was measured by passing through a dye cell. The fluorescence intensity from the dye cell was integrated along the beam incident direction. A closest Gaussian distribution was then fitted to the integral intensity profile and used to correct for laser sheet inhomogeneities.

For the PDA data, statistics were calculated for each probe position. Locations with data less than 50 counts (an average sampling rate $< 1.7\,s^{-1}$) were excluded. For some measurements, the PDA data at each location were classified by the size in the ranges [0, 10), [10, 40), [40, 80), and [80, 100) μm and the average velocities conditioned on the size category were reported. Data with few counts (<10) for each category were omitted.

3. Results and discussion

This section presents results on the structure and stability of turbulent swirl-stabilised spray flames at conditions far from, close to blow-off, and at the blow-off event. First, the blow-off limits are shown. Next, PDA results are discussed for the four fuels. Following that, images from OH*, OH-PLIF, and Mie scattering are shown and discussed. The lift-off height statistics and the topology of the OH islands are determined as additional measures that can help with the validation of combustion models focusing on capturing extinction.

3.1 Stability limits

Figure 2 shows the LBO limits obtained for the current set-up. 'E1', etc. (horizontal direction) stands for different fuel flow rates, while 'S' and 'B' indicate stable condition and blow-off condition, respectively. 'S1', 'S2' (vertical direction) stands for different air flow rates (and hence distances from the blow-off condition). The stable flames are shown with open symbols. Because of the stochastic nature of blow-off, the bulk velocity value at blow-off (U_B) in the figure is an average value of several blow-off events. The standard deviation of blow-off bulk velocities normalised by the MV is around 0.02.

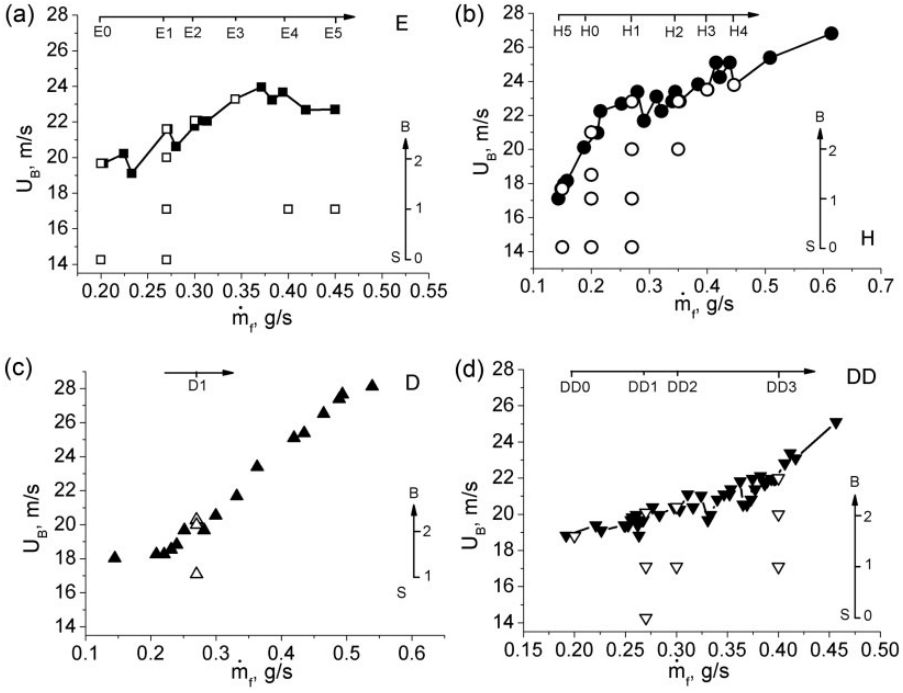

Figure 2. Blow-off velocities (closed symbols) as a function of fuel flow rate for (a) ethanol, (b) heptane, (c) decane, and (d) dodecane. Open symbols mark various test conditions of stable flames discussed in the text. The ticks on the lines at the top and right mark the fuel flow rate and air velocity, respectively, of the indicated flame code.

The trend of the blow-off limit for each fuel is consistent. In general, as the fuel flow rate ($\dot{m}_f$) increases, the blow-off air velocity increases, especially for the flames of the low-volatile fuels (n-decane and n-dodecane), for which the positive correlation observed between U_B and ($\dot{m}_f$) is stronger. A slightly different behaviour is shown in the blow-off curves of the more volatile fuels (ethanol and n-heptane), where U_B seems to present a levelling off in the intermediate fuel mass flow rate (0.35–0.45 g/s for ethanol flames, 0.2–0.35 g/s for heptane flames). This trend for heptane was also observed by Cavaliere et al.[5]

Several well-known blow-off correlations (premixed: Radhakrishnan et al.;[44] non-premixed: Broadwell et al.;[53] spray: Ateshkadi et al.[3]) could be applied to the current flames to collapse the blow-off data from various fuels. The correlation proposed by Radhakrishnan et al.,[44] originally developed for the blow-off of turbulent bluff body premixed flames, has also been used successfully for limited heptane data and for both premixed and non-premixed methane flames by Cavaliere et al.,[5] and here its accuracy is explored further for the present experiments that involve more liquid fuels. This correlation is based on a conceptual picture of combustion in small-scale (Kolmogorov) turbulent structures. The blow-off was deemed to occur when the time ratio $1/Da_1$ predicted by equation (2) exceeds a critical value (R_τ)

$$\frac{1}{Da_1} = \frac{\tau_c}{\tau_e} = \left[\frac{U_B \nu}{L}\right]^{1/2} S_L^{-1} > R_\tau \qquad (2)$$

where τ_c is the chemical time; τ_e is the eddy time as characteristic turbulent flow time; and ν is the kinematic viscosity, which is evaluated at the unburnt reactants conditions for premixed systems but at a temperature halfway between the reactants and the adiabatic flame temperature for sprays, as tested by Cavaliere et al.[5] following the suggestion by Mellor.[66] S_L is the laminar flame speed, evaluated at the premixed mixture equivalence ratio for premixed flames but at stoichiometry for non-premixed and spray flames; L is a characteristic size of the recirculation zone taken here as the bluff body diameter. The values of $1/Da_1$ of the current experimental data calculated from equation (2) are plotted in Figure 3. The correlation ratio lies in between 0.83 and 1.21 for all the fuels investigated at different fuel loadings. The mean critical value is around 0.95 among all the flames, with a standard deviation of 0.10. The difference between the maximum and minimum value for all the flames is around 0.38. The ratio is increasing with fuel loading for all fuels and a single critical value may be thought to emerge but only within 40%. Therefore, equation (2) cannot be used to better accuracy than this for the prediction of the blow-off condition.

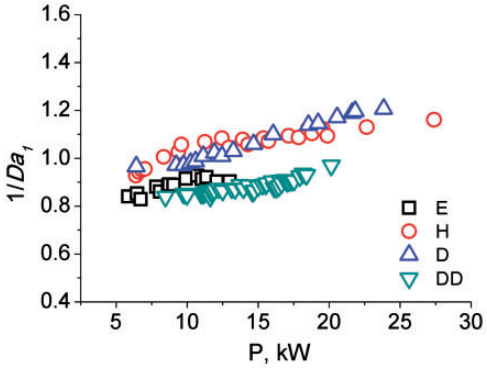

Figure 3. The blow-off limits correlation for the four fuels studied in this work (E – ethanol; H – heptane; D – decane, and DD – dodecane), calculated with the method proposed by Radhakrishnan et al.[44]

3.2 Flame appearance

Figure 4 shows photographs of stable flames for the four fuels. A typical feature of all flames is a double structure, with an inner region aligned with the spray cone and forming an apex at the injector, and an outer flame attached to the corner of the bluff body. The ethanol flame is purple-blue, while the others appear overall blue and with soot, which increases as the

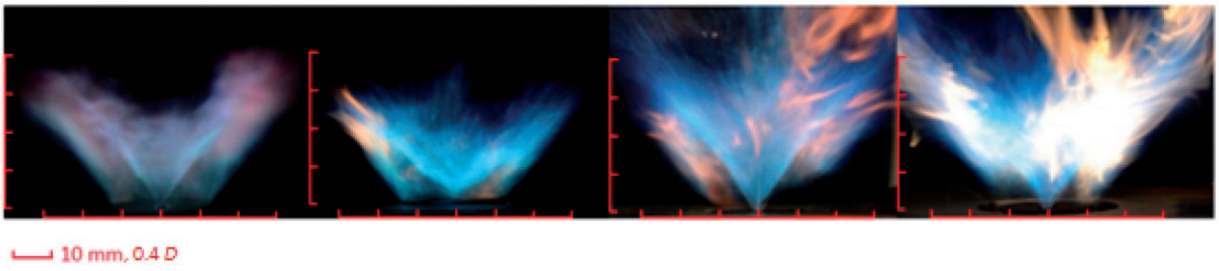

Figure 4. Photographs of stable spray flames of (from left to right) ethanol at E1S1, heptane at H1S1, n-decane at D1S1, and n-dodecane at DD1S1 (for all, $\dot{m}_f = 0.27$ g/s and $U_b = 17.1$ m/s, $Re_g = 13466$). D is the diameter of the bluff body.

molecular mass of the fuel increases. The soot-containing region seems to lie between the inner and the outer flame branches, and from above the bluff body surface to the flame tip downstream.

The inner flame zone appears a little lifted from the injector exit, especially for the ethanol flames. For decane and dodecane, the first millimetre of the conical spray is also evident (illuminated by the flame itself). There is also a slight asymmetry in the images of the heavy fuels, which could be related to a small lack of symmetry of the spray visualised by instantaneous Mie images of the corresponding reacting flow (discussed later). However, the spray statistics (size, velocity) are overall symmetric, as shown from the PDA measurements presented in Section 3.3.

The outer flame zone starts from the bluff body edge and shows intermittent lift-off, which will be quantified through analysis of the OH-PLIF images in Section 3.6. The flame height estimated from direct imaging for the four stable flames is in between 40 and 50 mm (1.6–2D) in general. The stable flame height of decane and dodecane is higher than that of the other fuels, probably because the spray traverses a longer length due to a larger mean droplet size (given by PDA measurements discussed in Section 3.3) and the lower volatility.

3.3 Droplet size and velocities

Figures 5 to 8 show the results from PDA measurements for stable flames far from and close to blow-off for the four fuels. Some additional data can be found in Yuan.[40] Figure 5(a) shows the radial distribution of SMD (also noted as D_{32}) measured at four different axial distances (Z) corresponding to (0.4, 0.8, 1.2, 1.6) Z/D, (D is the bluff body diameter), in two stable ethanol flames at conditions far from (E1S1) and close to (E1S2) blow-off, respectively. The two cases have the same fuel flow rate but different air bulk velocities. For all Z/D, only few droplets exist at radial locations larger than 1.2D. At small Z/D, the location of the peak SMD is aligned with the hollow cone spray path, where the maximum data rate is also observed. At longer distances downstream, the SMD is more uniform, with a smaller value obtained at locations close to the flame zone. The SMD measured for the two conditions (E1S1 and E1S2) is similar with the peak value close to spray jet around 70–80 μm, although a smaller SMD is obtained at outer flame zone (i.e. $x/D \approx 0.56$, $Z/D = 0.4$) at the lower velocity case (E1S1). This may be due to the more complete combustion that provides faster evaporation. In addition, a larger SMD value is found at downstream locations. This is reasonable as

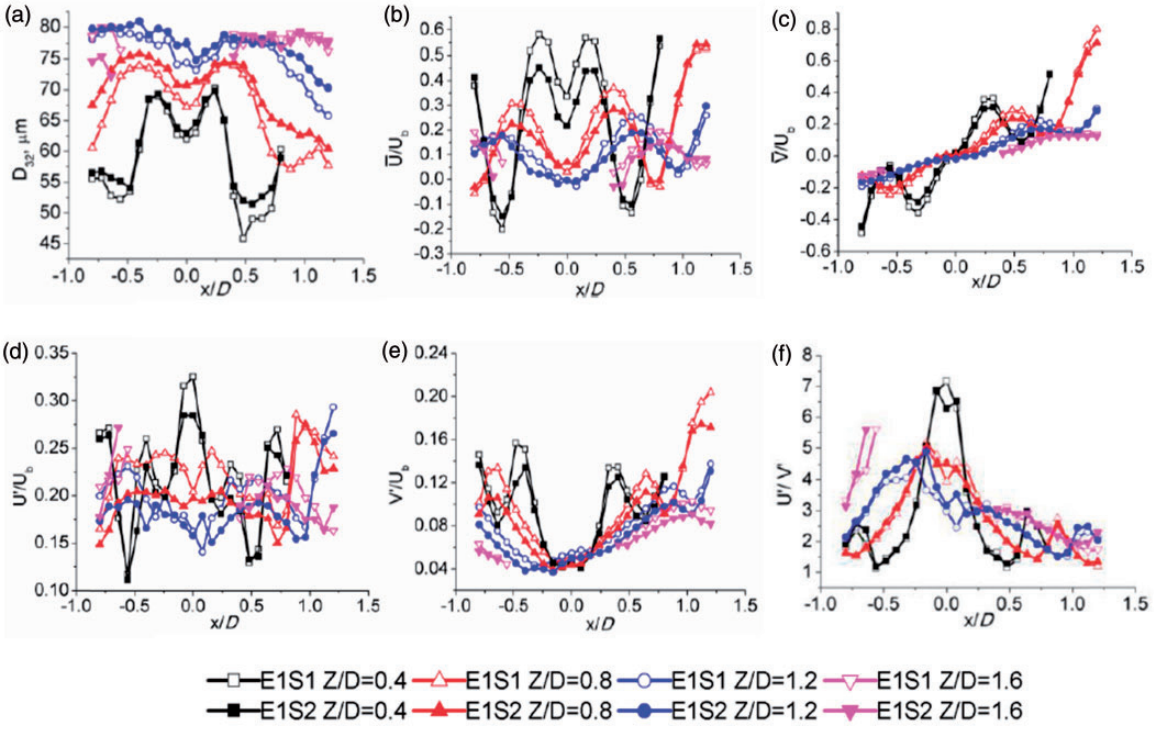

Figure 5. Distributions of (a) SMD, and normalised droplet mean (b) axial and (c) radial velocity, normalised rms fluctuations of (d) axial and (e) radial velocity, and (f) the ratio of the two velocity component fluctuations. Ethanol stable flames: E1S1 (open symbols) and E1S2 (closed symbols) at various downstream locations. E1S1 and E1S2 have the same fuel loading ($\dot{m}_f = 0.27$ g/s) and air velocity of 17.1 m/s and 20.0 m/s, respectively.

the droplets with a larger diameter have a larger inertia and travel further, while the droplets with a smaller diameter are mostly consumed by combustion or captured by the recirculating gases, both of which shift the SMD to higher values as we go downstream. Finally, we mention that a unimodal (Gaussian-like) distribution of droplet sizes was found at all the locations measured (not shown here). However, at high Z/D the size distribution for the larger SMD cases was slightly clipped at the cut-off (100 μm) from the PDA collection settings, which will result in the shown SMD underestimating the true MV.

Figure 5(b) shows that the droplet mean axial velocity ($\bar{U}$), for all Z/D, peaks at a location off-axis, and experience shows that this location overlaps with the maximum data rate location. At $Z/D = 0.4$ (black line), $\bar{U}$ is still positive at the centreline ($x/D = 0$). At higher Z/D, $\bar{U}$ along the centreline becomes close to zero, and the velocity probability density function becomes bimodal (not shown here). At $Z/D = 1.6$, very few droplets were collected at the axis and the region nearby. As we go outwards towards the annular air stream, $\bar{U}$ decreases and becomes negative at the flame zone, but further into the outer annular air $\bar{U}$ becomes positive. Along the vertical direction, $\bar{U}$ is maximised near the nozzle exit and decreases downstream. At the condition close to blow-off (filled symbols), $\bar{U}$ is smaller in the region inside of the annular jet compared to the condition far from blow-off (empty symbols) due to the fact that the spray is injected with the same velocity (since the fuel flow rate is the same), but the air velocity is higher and so is, presumably, the velocity of the recirculating gases that decelerate the droplets. Where the droplets are captured by the fast annular air stream, the droplet velocities are a similar fraction of the bulk air velocity for both cases. At these locations, all droplets are likely to follow the fast air flow (as also discussed later through conditional statistics). Figure 5(c) shows the droplet mean radial velocity ($\bar{V}$), which peaks at the spray cone trajectory axis and decreases towards the inner and outer flame brushes (also discussed later through Sections 3.4 and 3.5 of the flame HR and Mie imaging results). At further downstream ($Z/D = 0.8$ to 1.6), the remaining droplet past the outer flame zone flows outwards by the annular air flow.

Figure 5(d) and (e) shows the normalised rms fluctuations of the axial and radial velocities, respectively. The axial velocity fluctuations are higher at the axis and close to the annular air jet, while they are smaller close to the spray cone (Figure 5(d)). The radial velocity fluctuations are smaller at the axis and larger at both spray cone and annular air jet locations (Figure 5(e)). Figure 5(f) plots the ratio axial/radial rms fluctuations and it is clear that there is significant anisotropy, with the axial fluctuations being several times higher than the radial ones. This has been observed before in particle-laden inert jets,[67,68] attributed to the finite inertia of the carried phase, and in droplet-laden jets,[69] attributed additionally to ligament formation. In the present system, we may have a combination of these effects.

Figure 6 shows the profiles of mean velocity, conditioned on the droplet sizes at three size ranges: [10, 40) μm (estimated Stokes number 0.05–0.82), taken as the range most representative of the air flow since the small droplets are expected to follow the air, [40, 80), and [80, 100) μm. The unconditional $\bar{U}$ is also plotted as reference. Only few droplets were found in the range [0, 10) μm, thus the corresponding curve is not presented as it suffers from large statistical error. At the annular air stream the smaller droplets carried by the air stream tend to show a higher mean velocity than the larger droplets; however, the differences between the different droplet categories are much smaller than close to the axis (small x/D). Close to the axis, the small droplets have lower velocities than the larger ones, consistent

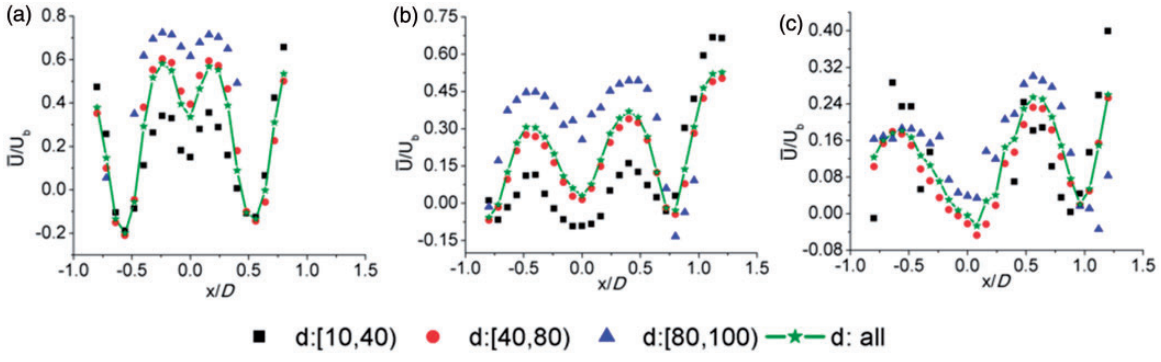

Figure 6. Mean axial droplet velocity conditional on the droplet size (square: 10–40 μm; circle: 40–80 μm; triangle: 80–100 μm) and the mean axial velocity using all droplets (star) versus radius, measured at various downstream locations (a: 10 mm; b: 20 mm; c: 30 mm). Ethanol stable flame EIS1 ($\dot{m}_f = 0.27$ g/s, $U_b = 17.1$ m/s). (a) EIS1 $Z/D = 0.4$, (b) EIS1 $Z/D = 0.8$, and (c) EIS1 $Z/D = 1.2$.

with the view that they are decelerated more by the opposing (recirculating) flow. At $Z/D = 0.8$, the small droplets have negative velocity, while the larger droplets have substantially positive velocity, which also explains the very large (unconditional) fluctuations of droplet axial velocity shown in Figure 5. At $Z/D = 1.2$, all droplet classes have similar velocities, possibly due to the fact that the initial high injection momentum has been eventually reduced due to drag and to the increase in the air velocity eddy scales that suggests that even larger droplets begin to follow the air flow.

Similar data for heptane are shown in Figure 7, but now the air velocity is the same and the fuel flow rate is changing. Figure 7(a) shows that the change in fuel loading has a minor effect on the droplet SMD, although a very small decrease can be seen in the higher fuel mass flow rate (H0S0). The difference in mean axial velocity (Figure 7(b)) is more obvious, with $\bar{U}$ increasing with fuel flow rate, suggesting that the spray penetrates more for the large fuel flow rate case. It is also suggested from Dumouchel[70] that SMD decreases as We_l increases (H0S0), consistent with the present measurements. In addition, as the initial droplet velocity increases with fuel loading, the droplet residence time is shorter in case H0S0 and hence a higher $\bar{U}$ is probably expected at downstream locations. The radial velocity component is also smaller at the flame with the lower fuel flow rate (Figure 7(c)). The fluctuations of the two velocity components are also plotted in Figure 7(d) to (f). The results are consistent with the previous discussion around Figure 5(d) to (f).

A notable difference between the ethanol and the heptane flames is the absence of droplets close to the centreline for the heptane flame. The measurements suggest that the atomiser behaves truly as a hollow cone atomiser for heptane but not so for ethanol, which gives droplets with significant positive axial velocity along the centreline. The differences between the four fuels are further highlighted in Figure 8. Note that the droplet size and velocity in the corresponding cold flow would have different distributions due to the different atomisation, but this is not addressed here, since the PDA instrument cannot provide data in the very dense, early region of the spray. Close to the nozzle, there is evidence of droplets from the ethanol flame at the centreline and the ethanol and heptane SMD is somewhat smaller compared to the other fuels that tend to have similar SMD. At large Z/D, all fuels show very similar SMD, suggestive of large droplets that have penetrated the inner flame zone, but at $Z/D = 1.2$ even the ethanol droplets have disappeared from the centreline. The SMD decreases in the radial direction as we approach the flame sheet.

Next, the mean axial velocity ($\bar{U}$) profiles are shown in Figure 8(e) to (h) at four downstream stations. In general, the high volatility fuels (ethanol and heptane:

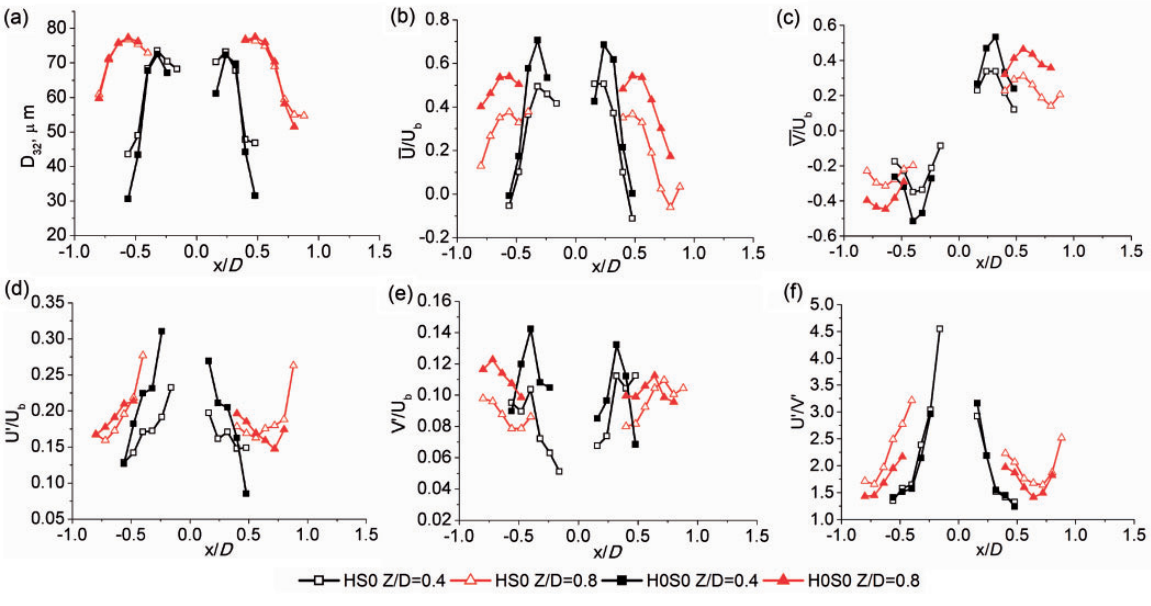

Figure 7. Distributions of (a) SMD, and normalised droplet mean (b) axial and (c) radial velocity, normalised rms fluctuations of (d) axial and (e) radial velocity, and (f) the ratio of the two velocity component fluctuations. Heptane stable flames: HS0 (open symbols) and H0S0 (closed symbols) at various downstream locations. HS0 and H0S0 have the same air velocity of 14.3 m/s ($Re_g = 11222$) and different fuel loading of 0.15 and 0.20 g/s (corresponding to We_l of 339 and 602), respectively.

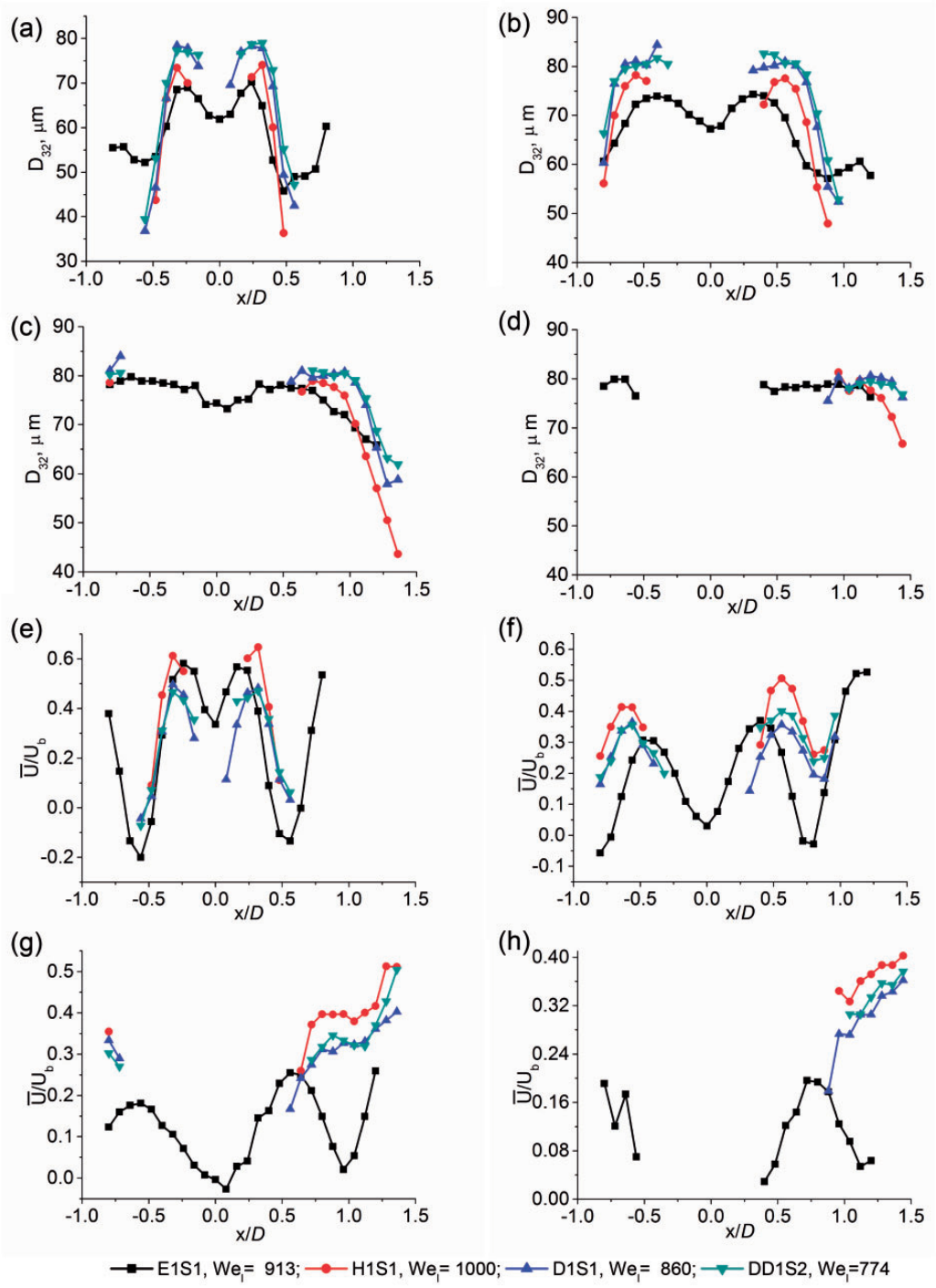

Figure 8. Comparison of the SMD (a)–(d) and normalised mean axial velocity (e)–(h) of the ethanol (E1S1, square), heptane (H1S1, circle), decane (D1S1, up triangle), and dodecane (DD1S1, down triangle) flames at (a, e) z = 10 mm, (b, f) z = 20 mm, (c, g) z = 30 mm, and (d, h) z = 40 mm. The fuel and air flow rates are identical for all flames ($\dot{m}_f = 0.27$ g/s, $U_b = 17.1$ m/s). The liquid Weber number is indicated. (a) $Z/D = 0.4$, (b) $Z/D = 0.8$, (c) $Z/D = 1.2$, (d) $Z/D = 1.6$, (e) $Z/D = 0.4$, (f) $Z/D = 0.8$, (g) $Z/D = 1.2$, and (h) $Z/D = 1.6$.

black and red symbols) have a higher peak velocity around the spray jet than the less volatile ones for all Z/D. However, the peak $\bar{U}$ of the ethanol spray decreases with distance faster than the other fuels. The heptane spray has an overall highest peak $\bar{U}$, which is consistent with the estimated jet exit velocity U_l shown in Table 2. Finally, downstream ($Z/D = 0.8$, 1.2), droplets survived from the outer flame zone are seen to have an increased $\bar{U}$ as they are captured by the annular air stream.

3.4 Stable flame and unstable flame before the blow-off event

In this subsection, the instantaneous and mean OH* images, the instantaneous and mean OH-PLIF images, and the Mie scattering images are discussed for each fuel at conditions far from blow-off and for the blow-off condition. For the latter, data are used from parts of the recordings before the final extinction event, which is separately discussed in subsection 3.5. We also discuss the effect of fuel type and fuel loading. The mean HR can be estimated from the inverse Abel transformed mean OH* chemiluminescence images. For non-premixed and spray systems the quantitative nature of chemiluminescence is questionable, hence here we use OH* only to infer the flame shape and location. Similarly, the OH-PLIF is not quantitative, but can be used to provide visualisation of the flame sheet. Finally, the Mie scattering is used only in a qualitative manner to demonstrate where the spray is.

3.4.1 HR. Figure 9 shows mean and instantaneous OH*, OH-PLIF, and Mie scattering for stable and unstable flames for the four fuels. The double structure of the HR zone is evident for all fuels and for all conditions: there is an inner flame and an outer flame, with the spray roughly between the two. The inner flame seems quite close to the spray, while the outer flame sheet is further outwards in the radial direction and is anchored to the corner of the bluff body in the mean. In an instantaneous basis, the inner sheet can be lifted from the apex of the spray and the outer sheet can be lifted from the corner of the bluff body.

The mean HR zone is, in general, thin and becomes thicker at unstable (blow-off) conditions. The ethanol flame's (Figure 9(a) and (e)) OH* emission is lower than that from the other fuels and the length of the HR zone is shorter, which is also supported by the PDA results shown in Figure 8 that $\bar{U}$ is smaller for the ethanol flame, especially at farther downstream locations. The angle of the inner HR branch seems narrower for ethanol flames than for the others, in agreement with the previous PDA results that show a narrower ethanol spray profile.

The mean HR region of the unstable flames (Figure 9, row 7, 10) is shorter compared to the corresponding stable flame, with the outer HR zone appearing more attached to the bluff body surface. The inner HR zone is smaller in size and has lower emission intensity, while the outer HR is widened. Instantaneously, the area of the HR region is smaller and appears non-axisymmetric, especially for the low-volatility fuels, for which almost half of the flame is missing, consistent with a wedge-like flame slowly moving around. This suggests the quenching of the flame in the inner recirculation zone (IRZ) for the flames at blow-off. The OH-PLIF and Mie images are discussed later, where the breaks of the OH sheet in the inner branch shown at blow-off conditions are consistent with the loss of OH* at the IRZ in both the mean and instantaneous OH* images. The instantaneous Mie images of unstable flames also present a non-axisymmetric profile of the spray, supporting the observation of single wedge-like HR regions shown in the instantaneous OH* images.

The mean Mie images show a more dispersed spray in the ethanol flames compared to the others and a slightly less disperse spray in the unstable flames (Figure 9(e) to (h) row 9, 12) compared to the stable flames (Figure 9(a) to (d) row 3, 6). The spray angles for all the conditions are similar at around 60°; however, a slightly narrower spray angle is found in the ethanol flames.

The effect of fuel loading is now examined. Figure 10 shows a clear difference of the mean HR location between different fuel loadings, suggesting the influence of spray atomisation and penetration on the main HR regions. This is in agreement with the conclusion from laminar flame calculations in Continillo and and Sirignano[56] and Dvorjetski and Greenberg[59] that the initial droplet velocity and size are critical to the spray flame structures in addition to the flow strain rate. The PDA results of the lowest fuel loading case (E0S0) also show a different pattern of size and velocity distributions, where the centreline has the maximum data rate and the peak $\bar{U}$, indicating a jet-like profile rather than a hollow cone spray profile. Also, We_l is lower ($We_l = 456$) for E0S0 so that the atomisation regime could be apparently different from the rest of the cases. From these HR images (a–d), it can be concluded that as the injection velocity increases (E0–E5), the distance of the inner branch from the nozzle exit decreases. A larger spray angle seems to be obtained at higher Weber number conditions of E4S1 and E5S1 than the low We_l cases of E0S0 and E1S0. The HR zones in E5S1 and E4S1 are similar and slightly longer for the higher injection velocity case (E5S1).

Figure 10(e) to (s) compares the influence of fuel loading on the mean HR zone of unstable flames of ethanol (e–j), heptane (k–p), and dodecane (q–s).

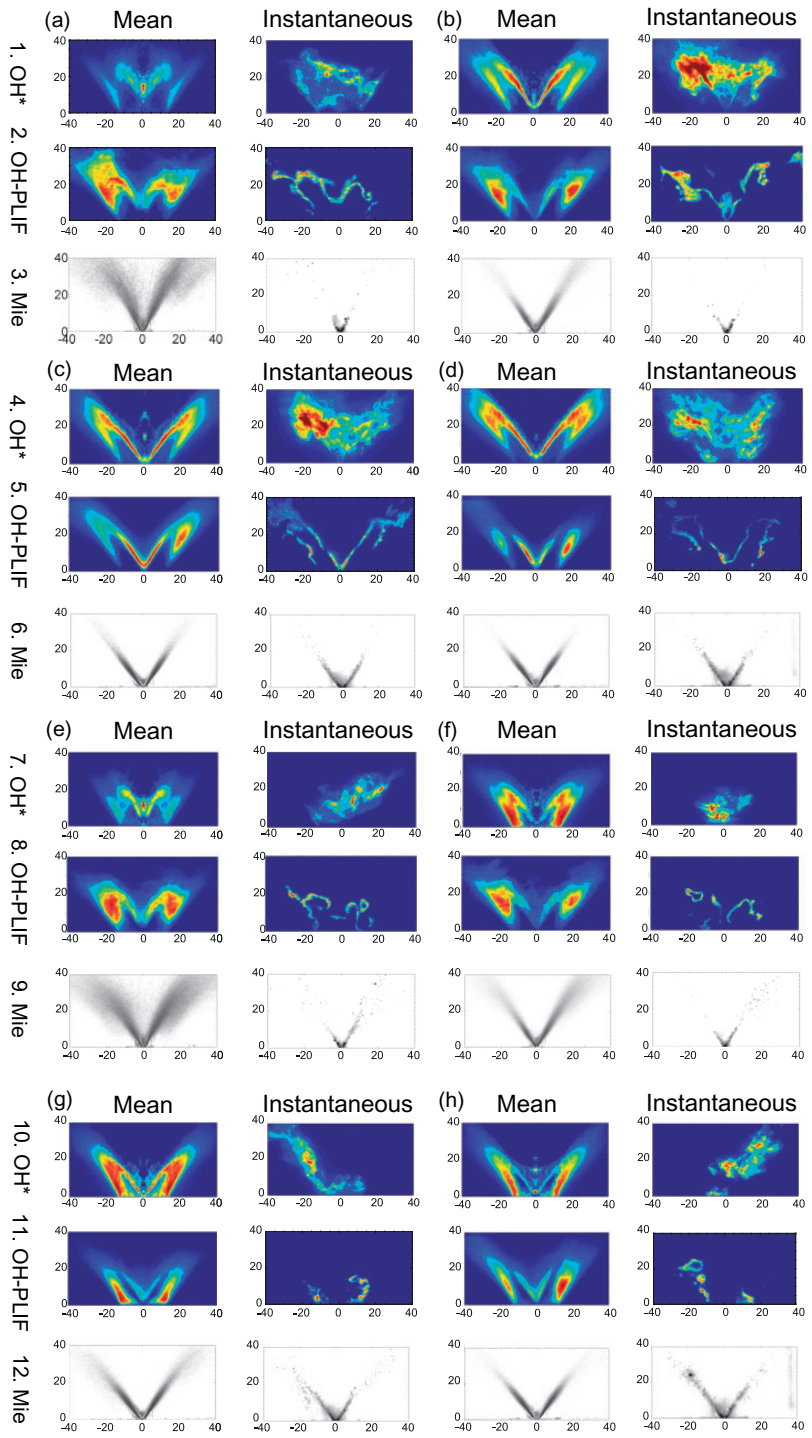

Figure 9. The mean and instantaneous images of OH* chemiluminescence (row 1, 4), OH-PLIF (row 2, 5), and Mie scattering (row 3, 6) from different stable flames (a)–(d) of ethanol (E1S1), heptane (H1S1), decane (D1S1) and dodecane (DD1S2), and unstable flames (e)–(h) of ethanol flame E1B, heptane flame H1B, decane flame D1B, and dodecane flame DD1B at the blow-off condition, but using data before the blow-off event. The mean OH* image is shown after inverse Abel transform. All the flames above have the same fuel flow rate at 0.27 g/s, and the stable cases have the same air velocity of 17.1 m/s, while the unstable flame cases at blow-off conditions have bulk velocities as shown in Table 1. Same colour map per row. (a) E1S1, (b) H1S1, (c) D1S1, (d) DD1S2, (e) E1B, (f) H1B, (g) D1B, and (h) DD1B.

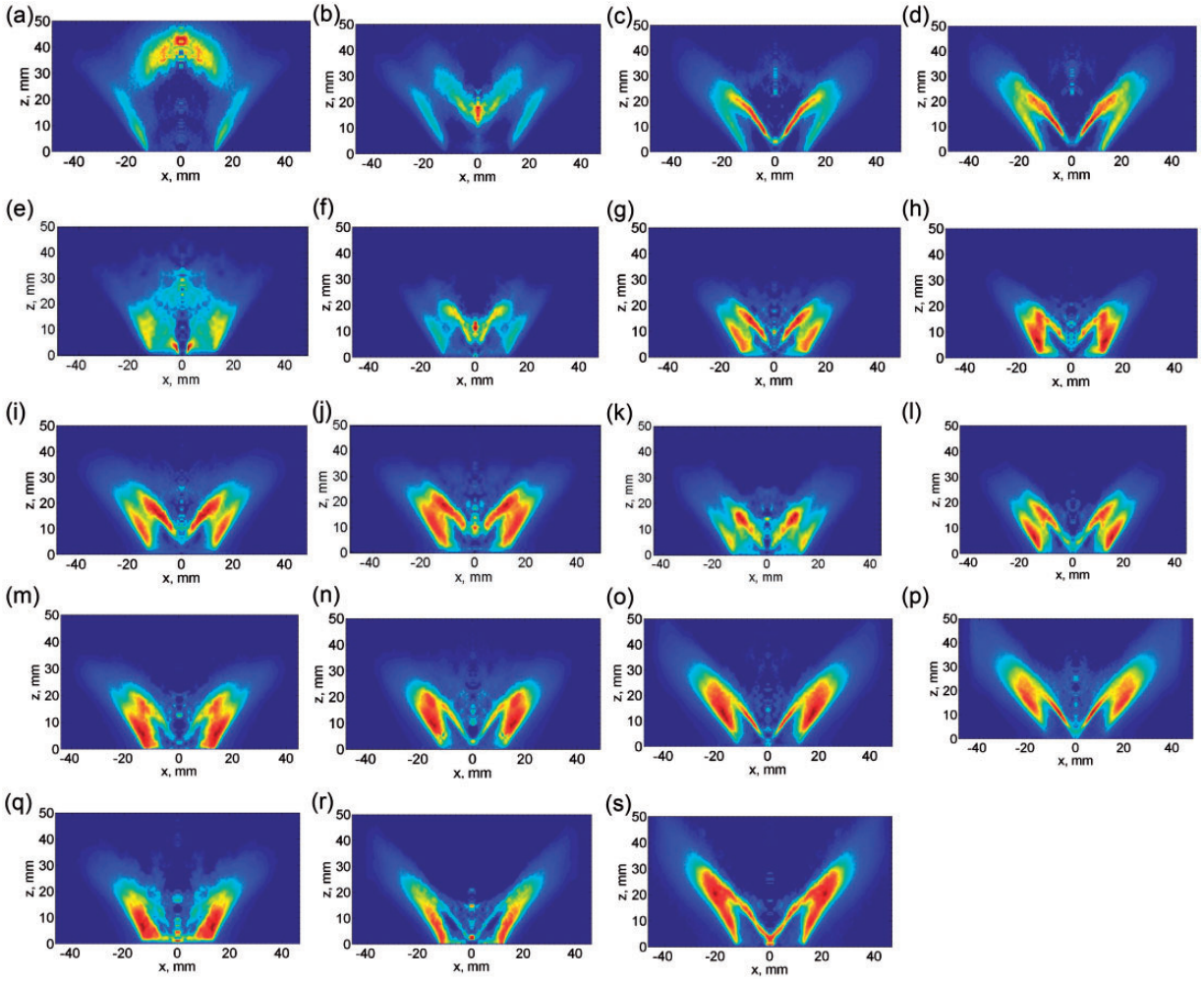

Figure 10. Inverse Abel transformed mean OH* chemiluminescence images for (a)–(d) stable flames of ethanol, and (e)–(s) flames at blow-off conditions ((e)–(j) ethanol, (k)–(p) heptane, and (q)–(s) dodecane). The corresponding fuel mass flow rate and air bulk velocities are shown next to the flame names. (a) E0S0 (0.2 g/s, 14.3 m/s), (b) E1S0 (0.27 g/s, 14.3 m/s), (c) E4S1 (0.4 g/s, 17.1 m/s), (d) E5S1 (0.45 g/s, 17.1 m/s), (e) E0B (0.2 g/s, 19.7 m/s), (f) E1B (0.27 g/s, 21.6 m/s), (g) E2B (0.3 g/s, 22.1 m/s), (h) E3B (0.35 g/s, 23.3 m/s), (i) E4B (0.4 g/s, 23.3 m/s), (j) E5B (0.45 g/s, 22.7 m/s), (k) HB (0.15 g/s, 17.7 m/s), (l) H0B (0.2 g/s, 21.0 m/s), (m) H1B (0.27 g/s, 22.8 m/s), (n) H2B (0.35 g/s, 22.8 m/s), (o) H3B (0.4 g/s, 23.5 m/s), (p) H4B (0.45 g/s, 23.8 m/s), (q) DD0B (0.2 g/s, 18.8 m/s), (r) DD1B (0.27 g/s, 20.1 m/s), and (s) DD2B (0.3 g/s, 20.4 m/s).

The fuel flow rates are indicated in Figure 10. The bulk velocities at blow-off are different (see Figure 2), but in general they increase with fuel flow rate. One of the common features of these unstable flames is a slightly larger area of the HR region with increasing fuel loading. In addition, the flames look more attached to the bluff body surface with a smaller fuel loading, for all fuels.

3.4.2 Flame sheet characteristics. The OH-PLIF signals were found to be correlated well with the main HR region in non-premixed hydrocarbon gaseous flames and heptane swirl spray flames.[39] Here the OH-PLIF data are further examined in the spray flames of the four fuels. Figure 9 (and later Figure 11) shows the images from fast OH-PLIF measurements of the stable and blow-off flames of each fuel. The average OH-PLIF images are first described (Figure 9) and reveal the main reaction zone locations of these swirl spray flames. The mean OH zone, in general, overlaps with the mean HR region represented by the mean OH* images and surrounds the spray visualised by the mean Mie images. The mean OH signal is very low (even below the detection threshold) at the anchoring point at the bluff body corner, suggesting flame lift-off there, which is clearly evident in the instantaneous OH-PLIF

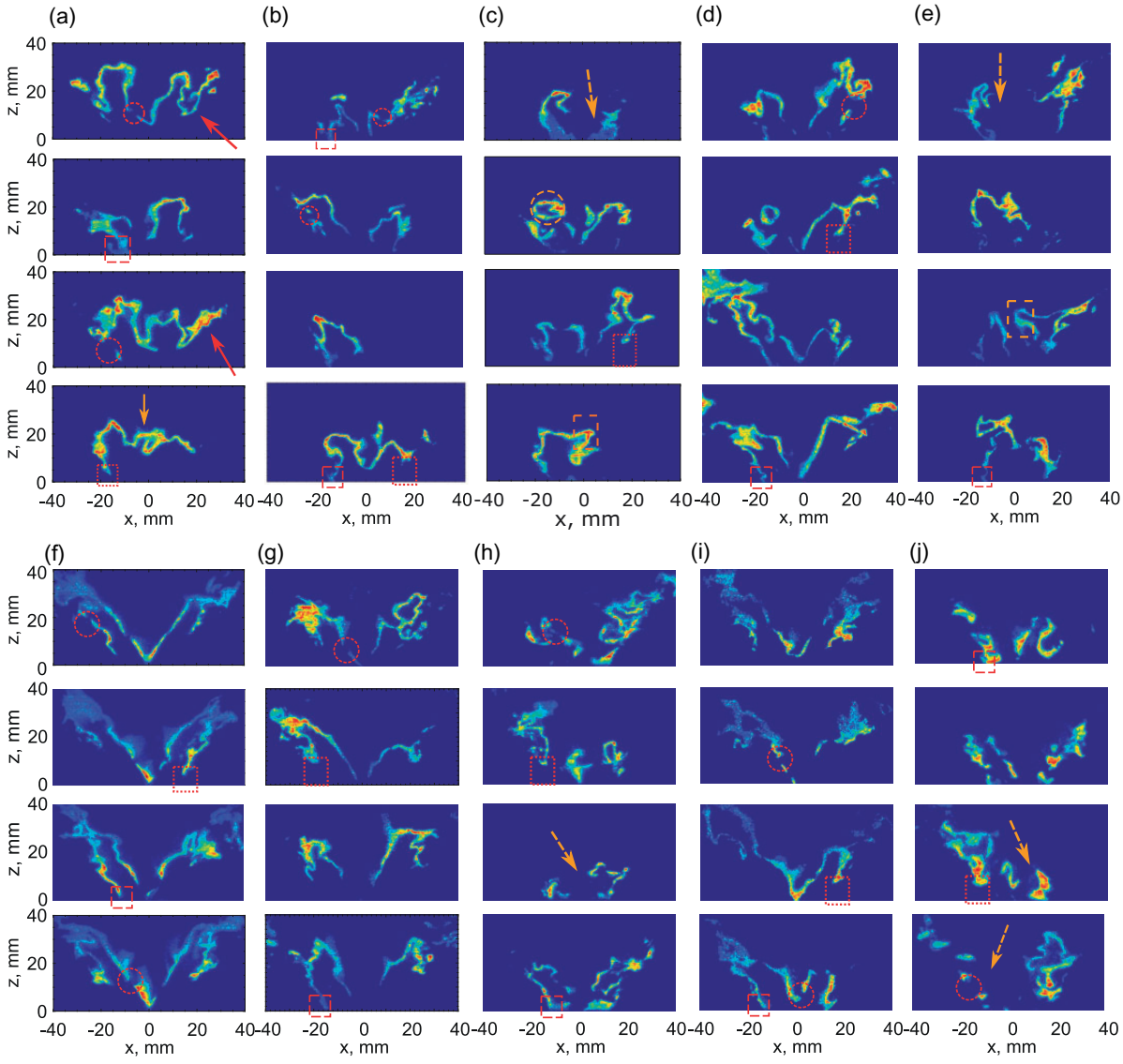

Figure 11. Instantaneous OH-PLIF images of (a, b, d, f, g, i) stable flames and (c, e, h, j) unstable flames at the blow-off condition before the blow-off event of (a)–(c) ethanol, (d) and (e) heptane, (f)–(h) decane, and (i) and (j) dodecane. The fuel flow rate is 0.27 g/s. Images not in sequence (same colour map for each flame). Dot-circle: breaks in inner or outer branch, dot-square: lift-off at bluff body edge, dash-square: attachment at bluff body edge, red arrow: divergence of outer OH branch, yellow arrow: lift of inner OH branch, yellow dash arrow: absence of inner OH branch, yellow dash rectangular: movement of inner OH branch, and yellow dash circle: spread of flame kernel. (a) E1S1, 17.1 m/s (79% of U_B), (b) E1S2, 20.0 m/s (93% of U_B), (c) E1B, 21.6 m/s (at U_B), (d) H1S1, 17.1 m/s (75% of U_B), (e) H1B, 22.8 m/s (at U_B), (f) D1S1, 17.1 m/s (84% of U_B), (g) D1S2, 20.0 m/s (98.5% of U_B), (h) D1B, 20.3 m/s (at U_B), (i) DD1S2, 20.0 m/s (99% of U_B), and (j) DD1B, 20.1 m/s (at U_B).

images. At blow-off conditions, the mean OH of the outer flame branch from all the fuels seems more attached at the bluff body edge and the OH-containing region is shorter. The inner flame branch seems shorter and unconnected with the outer branch for the low-volatility fuels. On an instantaneous basis, the stable flame is relatively continuous (albeit with breaks, especially along the outer branch), while the flame at blow-off is severely broken apart and fragmented, with the inner zone completely disappearing occasionally for the heavier fuels.

Figure 11 shows several instantaneous images of the OH radical for stable and unstable flames for all fuels. Starting with ethanol and with the flame far from blow-off (Figure 11(a)), it is evident that the OH region is overall thin and curved and continuous for its most

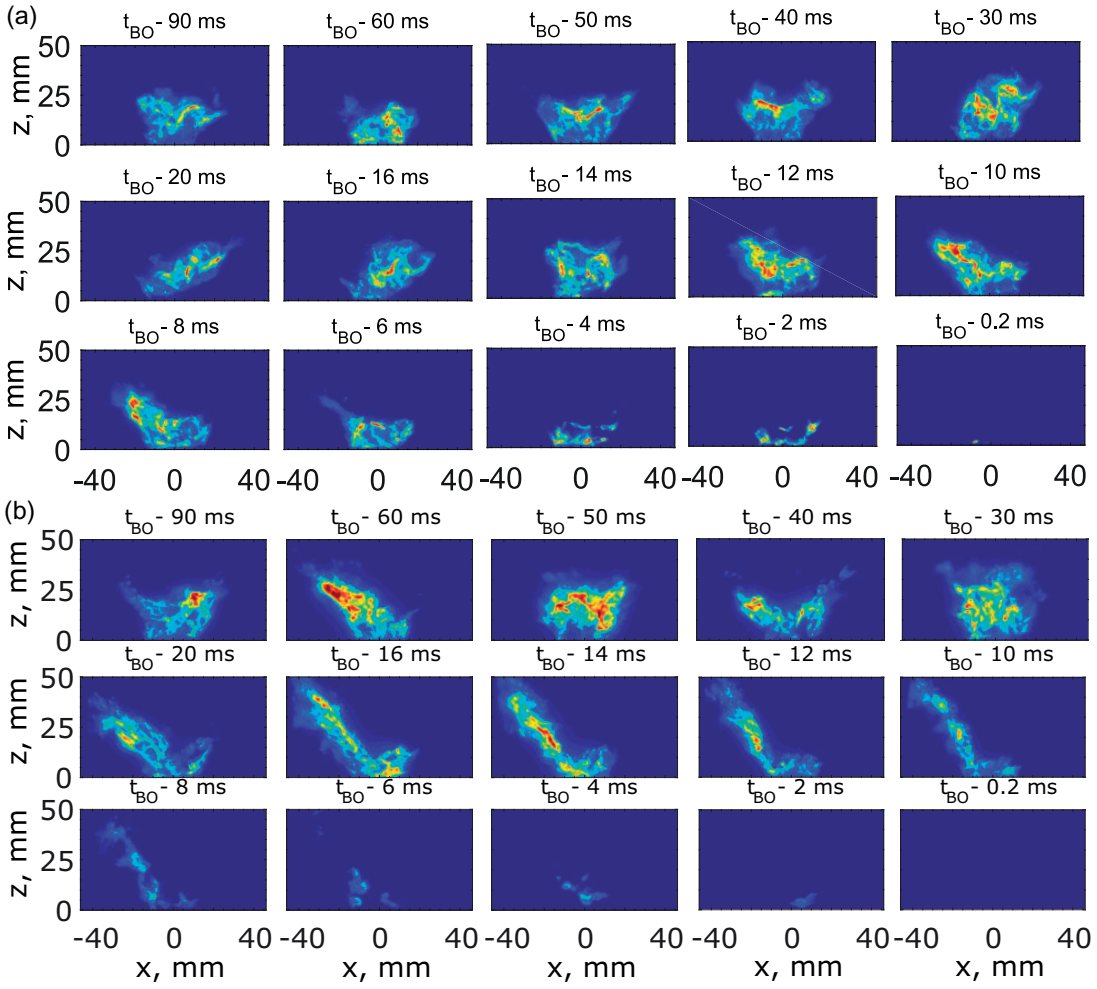

Figure 12. Instantaneous OH* images of swirl-stabilised spray flames of (a) ethanol, E1B, and (b) decane, D1B, at blow-off transient event (same colour map for each flame). The fuel flow rates of the four flames are the same, at 0.27 g/s. The relative time referenced to the time of complete disappearance of OH* is indicated on top of each image. (a) E1B, $U_B = 21.6$ m/s and (b) D1B, $U_B = 20.3$ m/s.

part, although there are occasional breaks at either inner or outer branch. A highly variable behaviour is seen between snapshots. The time evolution is not shown here, but playback of the movies shows that the sheet holes can close (i.e. we have reignition) and new local extinctions can develop. Due to the highly three-dimensional nature of the flow, however, further analysis of the speed of local extinction hole closing or opening, as pursued by Juddoo and Masri,[13] Meares et al.,[14] and Steinberg et al.[15] is not permitted in the present flame. At 93% of the extinction bulk velocity (Figure 11(b)), the degree of fragmentation is higher, more breaks are evident, and the length of the OH zone seems to have decreased compared to the flame farther from blow-off. Complete absence of a half branch can also be seen. The outer branch seems to be more often attached, however. At the blow-off condition, the OH is still thin and sheet like, but the degree of extinction is much higher than in the stable flames. The various features discussed above are marked in Figure 11: the absence of inner flame zone (Figure 11(c), arrow), the local extinctions (Figure 11(a) and (b), red circle), a spreading of a pocket of OH radicals downstream (Figure 11(c), yellow circle), attachment and lift-off at the bluff body edge (Figure 11(a) to (c), rectangles).

Data for heptane are shown in Figure 11(d) and (e). Similarly to ethanol, the stable flame OH sheet (Figure 11(d)) is thin, lifts off at the bluff body edge, and has breaks and closures. However, the inner OH branch looks more stable than ethanol's, presenting an overall 'V' shape. The unstable heptane spray flame (Figure 11(e)) also shows similar features, but a more variable behaviour is shown with large breaks and even complete absence of inner or the outer reaction zone. The results are consistent with the one reported previously[5] with a different atomiser.

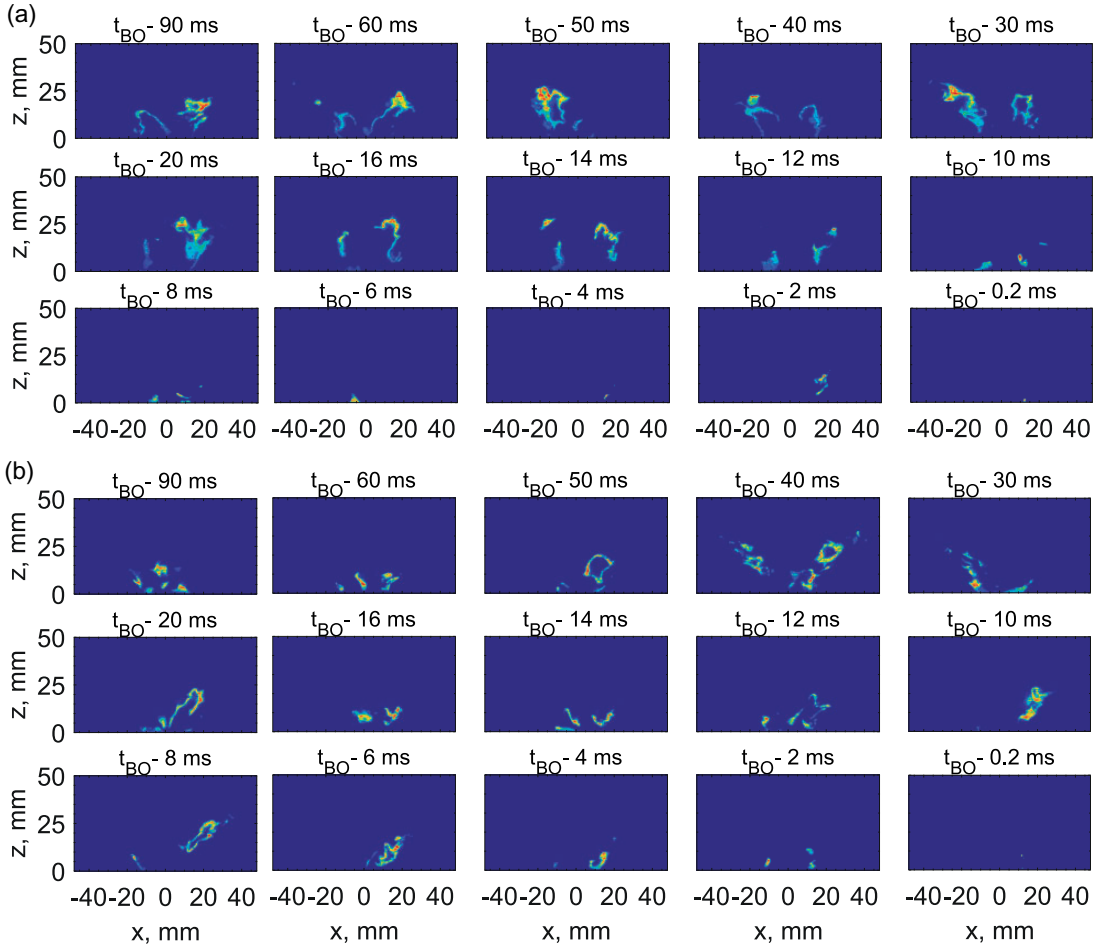

Figure 13. Instantaneous OH-PLIF images from flames of (a) ethanol, E1B, and (b) decane, D1B, during the blow-off event (same colour map for each flame). The fuel flow rate was 0.27 g/s and the velocity for each blow-off event is indicated. The relative time referenced to the time of complete disappearance of OH is indicated on top of each image. (a) E1B, $U_B = 21.6$ m/s and (b) D1B, $U_B = 20.3$ m/s.

The decane and dodecane flames are quite similar (Figure 11(f) to (h) and (i) and (j)). Far from blow-off, the OH sheets are relatively continuous, thin, with occasional breaks (circles) and lift-off (rectangles), and the inner flame is securely anchored to the spray nozzle. The OH region is well aligned to the hollow cone spray jet, probably due to the low volatility of the fuel that restricts the penetration of vapour into the recirculation zone. For the unstable cases (Figure 11(h) and (j)), both inner and outer branch show intense break-ups and the OH appears more attached to the bluff body surface; the inner reaction zone is apparently missing or shifts towards the outer shear layer.

3.5 *Unstable flame characteristics during the blow-off event*

In this subsection, the blow-off transient is discussed from the perspective of OH* and OH-PLIF evolution. A quantification of the duration of the blow-off event is also attempted based on the evolution of the OH* images. In the Supplementary Material, a movie of OH* of the blow-off transient for decane is given, which is typical of all fuels.

Figure 12 shows the sequence of OH* images of the blow-off event of the ethanol (E1B) and decane (D1B) flames. The corresponding OH* sequence of the heptane (H1B) and dodecane (DD1B) flames is plotted in Figure 20 of Appendix 1. The time line is referred to the instant of the flame's complete disappearance and is marked above the images. A gradual decrease of the size of the HR zone is observed and the last flame fragment is usually seen around the spray injection point. The images from the low-volatility fuels (decane and dodecane) present a distinctive asymmetric pattern, consistent with half the flame surviving in a wedge-like shape and rotating around the burner. Such a feature is not very prominent in ethanol or heptane.

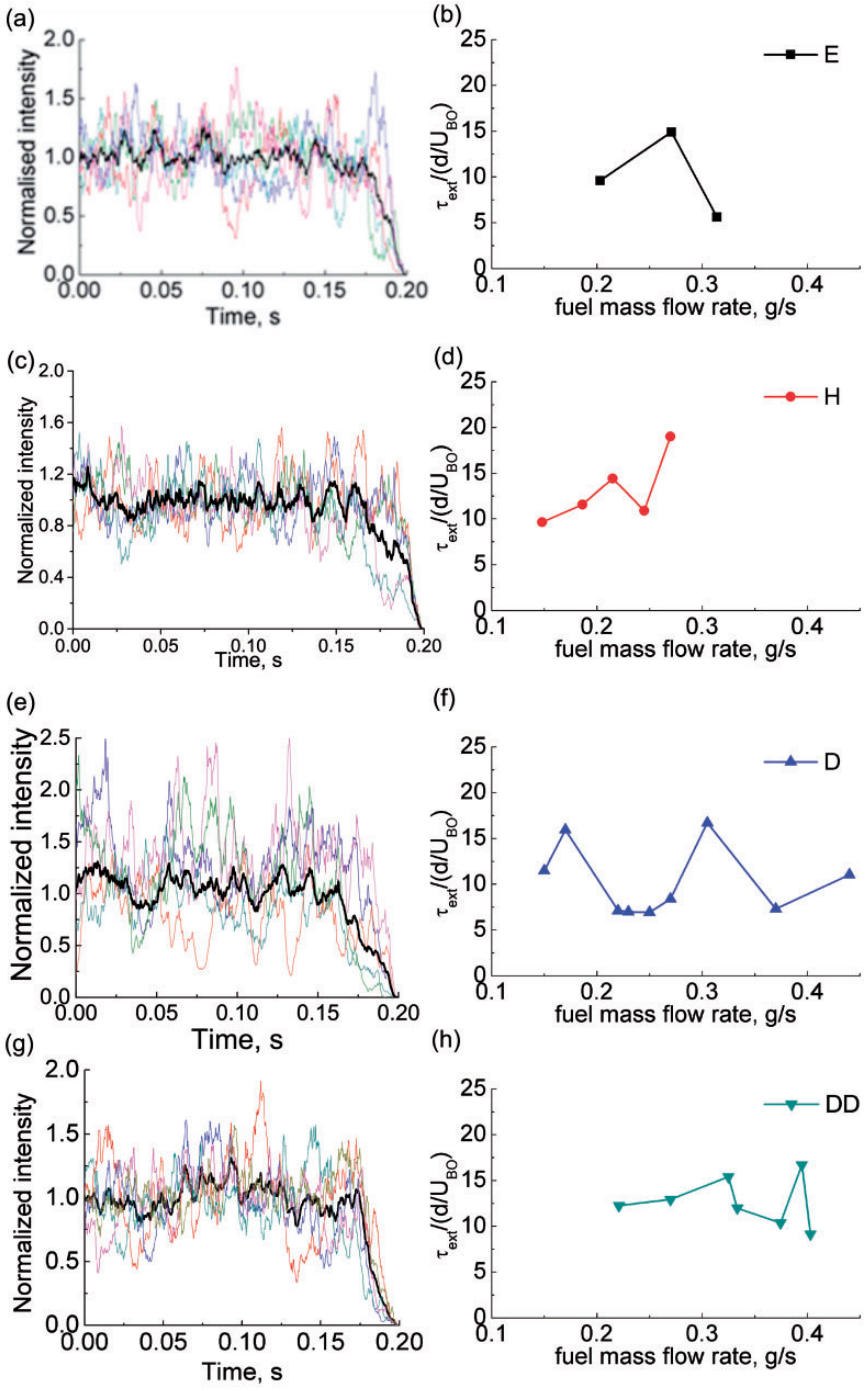

Figure 14. (Left) Integrated OH* during the blow-off event (the colour line stands for instantaneous time series, black line indicates the average value) and (right) the normalised transient duration at various fuel loadings of flames of (a, b) ethanol (flame E1B), (c, d) heptane (flame H1B), (e, f) decane (flame D1B), and (g, f) dodecane (flame DD1B). The fuel flow rate of (a), (c), (e), and (g) is 0.27 g/s. (a) E1B, $U_B = 21.6$ m/s, (b) ethanol, (c) H1B, $U_B = 22.8$ m/s, (d) heptane, (e) D1B, $U_B = 20.3$ m/s, (f) decane, (g) DD1B, $U_B = 20.1$ m/s, and (h) dodecane.

The low volatility could promote a lack of fuel vapour in the IRZ. The asymmetric wedge-like pattern is not seen clearly in stable flames, suggesting that the significant local quenching leads to the possibility of spray penetration there, diminishing further the generation of vapour at that part of the flame, breaking axisymmetry and resulting in a large local extinction that can rotate with the swirl or become a precessing structure. If the slow rotational motion of the wedge-like shape is related to the tangential flow component induced by

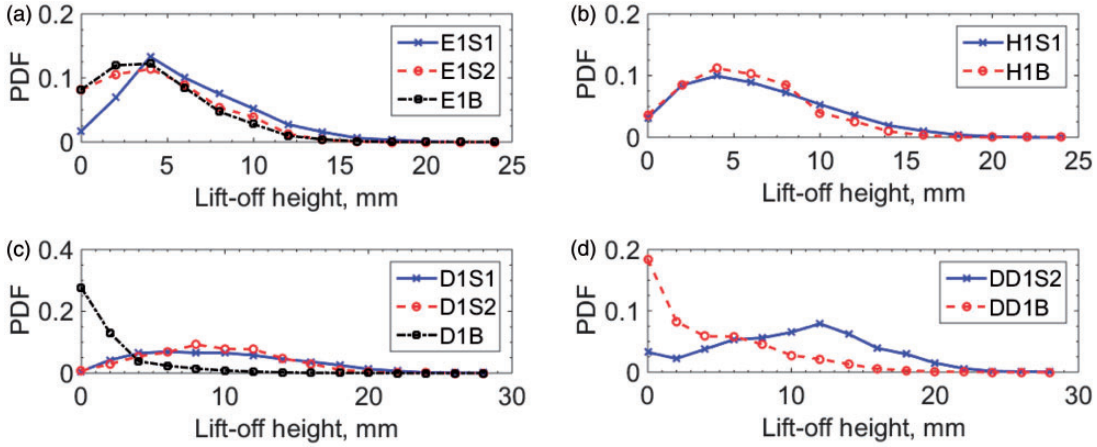

Figure 15. PDF of lift-off height of flames of (a) ethanol, (b) heptane, (c) decane, and (d) dodecane at different distances from the blow-off condition. The fuel flow rate for all the flames is 0.27 g/s. The flow parameters are listed in Table 1.

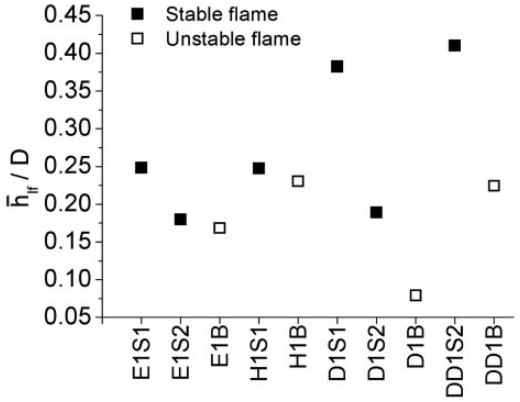

Figure 16. The average lift-off height normalised by the bluff body diameter for various flames. The fuel flow rate is 0.27 g/s and the air velocity for each flame is marked on Figure 2.

the swirl of the air flow, then an estimate of the frequency is as follows. The gas flow velocities measured (via LDA) from a previous work[71] in the same burner (heptane flow rate of 0.12 g/s and air bulk velocity (U_b) of 14.3 m/s) showed a normalised tangential velocity of (0.7 ± 0.003) U_b at the outer annular air locations of $0.96\,x/D$ (radius/bluff body diameter), and $0.40\,Z/D$ (downstream distance/bluff body diameter), which gives an angular frequency of 66 Hz. The tangential velocity of the spray in the current work shows a normalised value of 0.020 ± 0.0001 to the air bulk velocity in the spray jet path (corresponding to a rotational frequency of around 0.5 Hz) at the same downstream distance, which is small compared with the value of the gas. The transverse motion of this wedge-like shape is also picked up by an analysis with the Proper Orthogonal Decomposition method,[40] and a high energy content (around 20%) is found to be associated with this mode. However, the Fourier transform analysis of the time coefficient of this mode does not indicate a dominant frequency associated with this transverse motion, but broad peaks between 30 and 60 Hz. Therefore, the reasons why the flame assumes the shape it takes are not clear; simultaneous PIV/OH/Mie data might be useful in this respect.

Figure 13 shows the transient blow-off process from the OH-PLIF images of the ethanol (E1B) and decane (D1B) flames. The corresponding OH-PLIF sequence of the heptane (H1B) and dodecane (DD1B) flames is plotted in Figure 21 of Appendix 1. As the flame becomes fragmented, the out-of-plane motion makes interpretation of these images difficult. An absence of the inner branch is often observed at the blow-off transient process. The last fragment of OH radicals appears close to the bluff body. No significant differences are seen between the fuels.

Figure 14 plots several instantaneous (coloured line) and average (black line) time series of the normalised integrated intensity of OH* signals at blow-off conditions for the four fuels. The integral OH* gradually decreases before the blow-off event, but is relatively constant for some time before the blow-off event begins. (It was during this period that data were collected for the flame conditions denoted as 'blow-off' in Figures 9 to 11.) The characteristic duration of the blow-off event is estimated as the time needed for the integrated OH* to fall from 90 to 10% of the normalised value and is around 10–30 ms for all fuels. The average transient time, τ_{ext}, estimated from five individual blow-off events, is further normalised by the characteristic time flow expressed by D/U_B, at various fuel flow rates (and therefore with different U_B; Figure 2), and is plotted for different fuels in Figure 14. The values are in the same range as previously reported for heptane spray flames with

Table 4. Average lift-off heights of stable and unstable spray flames. The fuel flow rate $\dot{m}_f$ for each condition was 0.27 g/s.

Name	E1S1	E1S2	E1B	H1S1	H1B	D1S1	D1S2	D1B	DD1S2	DD1B
U_b (m/s)	17.1	20.0	21.6	17.1	22.8	17.1	20	20.3	17.1	20.1
U_b/U_B	79%	93%	1	75%	1	84%	98.5%	1	85%	1
$\phi_{overall}$	0.19	0.16	0.15	0.32	0.24	0.31	0.27	0.24	0.27	0.27
h_{lf}/D	0.25	0.18	0.17	0.25	0.23	0.38	0.19	0.08	0.41	0.22

a different atomiser.[5] No apparent trend is shown within each dataset for each fuel, and no trend is apparent across fuels. The mean transient duration is around 11 characteristic flow times using all data together. This normalised blow-off event duration is lower than the one for premixed (~38) and non-premixed methane flames (~37) reported previously[5] at the same burner, attributed in Cavaliere et al.[5] to a feedback mechanism concerning a spray in a progressively extinguishing flame: as the flame gets progressively smaller and therefore the IRZ cooler, evaporation is slower and so the burner is starved of fuel vapour, which accelerates the flame annihilation process. This makes the normalised extinction transient duration for the spray fame shorter than for gaseous fuelled flames.

A similarly estimated extinction time based on the OH-PLIF images is smaller, reaching only a few (4.5 in average) flow characteristic times D/U_B. This duration is roughly half of the blow-off transient time obtained from the OH* images discussed in Figure 14 and the difference can be understood by considering that OH* is a line-of-sight technique and so picks up emission from out-of-plane flame fragments that would not give rise to any OH-PLIF signal.

3.6 Lift-off height statistics and further metrics

Figure 15 shows the probability density function of the lift-off height, calculated in OH-PLIF images as the axial distance of the first emergence of OH in the outer flame branch for the bluff body corner. In general, the lift-off height decreases as the air bulk velocity increases, and at the blow-off condition the probability of the occurrence of flame attachment (zero lift-off height) increases. For ethanol, the mean lift-off height is 6.2 mm for E1S1 (79% of U_B), 4.5 mm for E1S2 (93% of U_B), and 4.2 mm for E1B (at U_B). The same trend is obtained for the other fuels as well (Figure 15(b) to (d)). The mean lift-off heights normalised by the bluff body diameter for the four fuels are plotted in Figure 16 and listed in Table 4. At the stable flame, the normalised average lift-off height is significantly larger for the lower volatility fuels (e.g. under the same air and fuel flow rates conditions, the value is 0.25 for the ethanol stable flame (E1S1) and is 0.41 for the dodecane stable flame (DD1S2)). At the blow-off conditions, no direct correlation is found between the lift-off height and fuel volatility or the overall equivalence ratio. These quantities are challenging targets for combustion CFD.

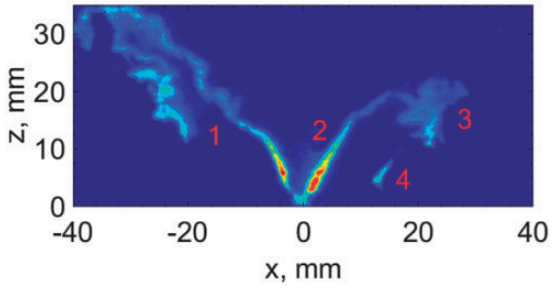

Figure 17. An example OH-PLIF image of stable decane flame (D1S1, fuel flow rate is 0.27 g/s and air bulk velocity is 17.1 m/s). The image includes four separated 'islands'. The total area of the binarised OH signal normalised by D^2 (D is the bluff body diameter) is 0.60. The circularity (F) of these subregions is 0.08, 0.25, 0.57, 0.32 for regions 1–4, respectively.

In an effort to produce some quantitative measure of the degree of local extinction from this single-scalar planar imaging, some further analysis of the OH-PILF images is discussed. From each OH image, after binarisation (detailed in Yuan[40]), two parameters are extracted: (i) the area, A, of a connected OH region ('island'); and (ii) the perimeter, P, of the OH region, which then gives the circularity index F, where $F = 4\pi A/P^2$ (the circularity index as defined is unity for a circular object and is zero for a line object). An example OH image is shown in Figure 17: four separate 'islands' (objects) are found, for each of which we calculate the above.

The averaged value of the above morphology metrics of the OH-PLIF images from the stable and unstable flames of the four fuels is shown in Figure 18. The mean object area decreases, while the circularity index increases at conditions approaching blow-off, suggesting that the OH images are more fragmented with increasing air bulk velocity towards blow-off. There is a slight trend of reducing circularity as the

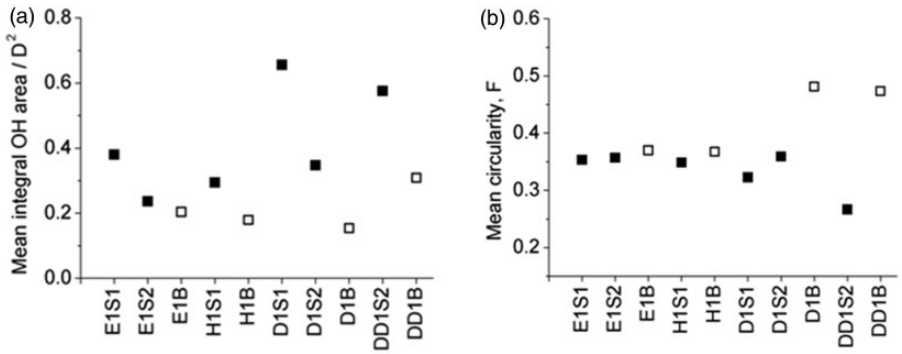

Figure 18. Morphology of the OH-PLIF images from the different flames: the average value of (a) normalised integral binary area, (b) the average circularity, F. Open symbols: unstable flames; closed symbols: stable flames.

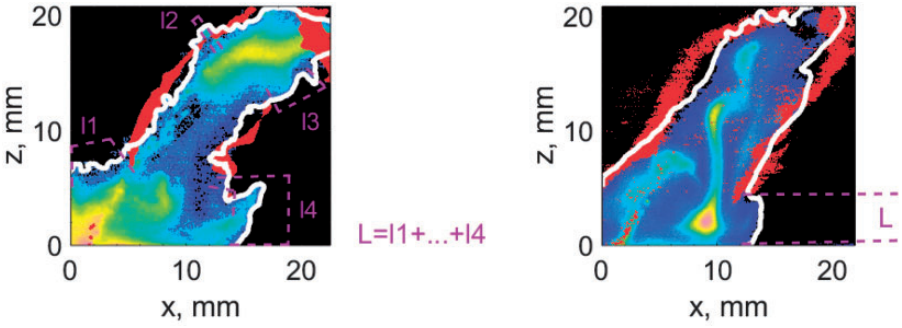

Figure 19. An example image from the joint CH_2O-OH PLIFs image of stable heptane flame (H1S1, fuel flow rate is 0.27 g/s and air bulk velocity is 17.1 m/s) from Yuan et al.[39] The image includes the binarised OH signal (red), CH_2O signal (colour, from blue-pink), and the CH_2O signal's boundary (white line), which can be used as a rough estimate of the stoichiometric contour.[39] L is measured as the length of the CH_2O boundary that has zero overlap with the OH signal. The total length of the CH_2O boundary (the white line) is calculated as Σ. The quenching percentage, b, of the stoichiometric iso-line is then obtained as L/Σ.

fuel volatility decreases, which is consistent with the qualitative observation that the decane and dodecane fuels tend to have OH sheets that are narrower and more aligned with the spray than the ethanol and heptane flames.

Finally, for the heptane flames only, the degree of local extinction was quantitatively estimated by reanalysing the data from Yuan et al.[39] where simultaneous CH_2O–OH PLIF was performed. In that reference, laminar flame simulations are discussed that suggest that the boundary of the CH_2O region can mark approximately the stoichiometric (ξ_{st}) iso-line. The simultaneous presence of OH along the ξ_{st} iso-line is then deemed to correspond to a reaction sheet, while absence of OH is deemed to correspond to a local extinction. An example image of the merged OH and CH_2O signals is shown in Figure 19 that demonstrates the method to obtain the quenched flame sheet length. Note that this processing method considers a lifted flame as extinguished all the way until the lift-off height discussed in Figure 15. However, it also includes breaks in the OH sheet from all locations. The CH_2O-PLIF technique was not successful for the ethanol flame due to significant parent fuel interference and availability of the instruments did not allow measurement with the decane and dodecane fuels, which must be attempted in the future.

From each image, the percentage of length of the estimated ξ_{st} iso-line that does not have OH is denoted by b. A total number of 400 instantaneous images were processed for two stable heptane flames: (1) H1S1 (far from blow-off), and (2) H1S2 (close to blow-off). The MV of b for H1S1 was 0.21 and the standard deviation was 0.136, while flame H1S2 had a MV of 0.34 and a larger standard deviation of 0.167. Therefore, the degree of extinction increases as the air bulk velocity increases, consistent with expectations from non-premixed jet and swirl flames.[10,13,21] Although the above estimate is approximate due to the uncertainty by which the CH_2O signal can truly mark the stoichiometric iso-surface, it can provide a further useful metric for modelling.

3.7 Implications for modelling

Gaseous piloted jet flames far from and close to blow-off have been studied extensively[13,22–25] for a range of fuels, and a key finding is that the degree of local extinction increases as we approach the blow-off velocity. In the jet flames, a key characteristic is the reignition allowed by the strong pilot, the relaxation of the strain rates as we go downstream along the jet, and the dominant convective motion. In a parallel effort, swirling non-premixed flames have also been explored experimentally,[10,11] and most of these experiments were focused on conditions where the fuel jet is important and the flame is relatively long compared to the size of the stabiliser. Similar efforts for jet spray flames are also becoming available.[41,69,72] The above experiments have provided very challenging datasets for model validation and, recently, the focus on LESs has provided the opportunity to also validate the dynamic behaviour of the local extinction[73] and not only the averaged degree of burning.[30,74,75]

The present data, which consider recirculating spray flames with local extinction and which provide time-averaged statistics and transient information, can be thought of as offering additional validation data for extending modelling efforts towards capturing limiting phenomena in practically important geometries and for a range of liquid fuels. The relevant data from the present work that can be used as target quantities for combustion model validation include: the blow-off condition (Figure 2), which is a quantity that is still very difficult to predict with combustion CFD; the flame fragmentation (Figures 11 and 18), the lift-off height statistics (Figures 15 and 16; Table 4), and the estimated degree of local extinction (Figure 19 and related text), which are challenging but useful metrics for validating predictions of local extinction; and the blow-off transient duration (Figure 14) that can help assess the accuracy of predicting combustion transients.

4. Conclusions

This work discussed experimental observations with swirling spray flames at conditions far from blow-off, close to blow-off, at the blow-off condition before the final blow-off event, and during the final blow-off transient. Four different fuels were studied, two considered of high volatility (ethanol, heptane) and two considered of low volatility fuels (decane and dodecane). It is shown that the flame location is affected by the fuel type. The low volatility fuels show a longer penetrating length of the droplets and a slightly larger mean droplet size with a smaller dispersion of the spray, ensuring a longer, straighter, more anchored flame sheet represented by the OH* and OH-PLIF images. The stable flames are intermittently lifting at the bluff body edges, with the average lift-off height decreasing as the air velocity increases and as fuel volatility increases. Fewer breaks are shown in the IRZ flame than in the outer shear layer for stable flames, but the occurrence of inner branch quenching increases at blow-off. The intense local extinction eventually leads to the global blow-off of the spray flame. The asymmetry of the instantaneous OH* and OH-PLIF images of decane and dodecane flames is more prominent at blow-off than at stable conditions and for ethanol and heptane flames. The transient blow-off process revealed from OH* images lasts a few tens of milliseconds, corresponding to an average value around 11 times the characteristic flow time scale, relatively smaller than the one for premixed and non-premixed methane flames examined previously with the same burner.

Due to the focus on local and global extinction and the flame transient behaviour, the present data provide a new validation test case for combustion CFD with models that can capture unsteady flame behaviour and extinction, such as LES with advanced turbulent combustion models.

Declaration of Conflicting Interests

The author(s) declared no potential conflicts of interest with respect to the research, authorship, and/or publication of this article.

Funding

The author(s) disclosed receipt of the following financial support for the research, authorship, and/or publication of this article: This work has been partly funded by the EPSRC through a Dorothy Hodgkin Studentship and grant EP/J021644/1, and partly by Rolls-Royce.

ORCID iD

Epaminondas Mastorakos http://orcid.org/0000-0001-8245-5188

References

1. Ballal DR and Lefebvre AH. Weak extinction limits of turbulent heterogeneous fuel/air mixtures. *J. Eng. Gas Turbines Power* 1980; 102: 416–421.
2. Plee SL and Mellor AM. Characteristic time correlation for lean blowoff of bluffbody-stabilised flames. *Combust. Flame* 1979; 35: 61–80.
3. Ateshkadi A, McDonell VG and Samuelsen GS. Lean blowout model for a spray-fired swirl-stabilised combustor. *Proc. Combust. Inst.* 2000; 28: 1281–1288.
4. Marinov S, Kern M, Zarzalis N, Habisreuther P, Peschiulli A, Turrini F and Sara ON. Similarity issues of kerosene and methane confined flames stabilized by swirl in regard to the weak extinction limit Flow. *Turbul Combust* 2012; 89: 73–95.
5. Cavaliere DE, Kariuki J and Mastorakos E. A comparison of the blow-off behaviour of swirl-stabilized

premixed, non-premixed and spray flames. Flow Turbul. *Combust* 2013; 91: 347–372.
6. Lefebvre AH. *Gas Turbine Combustion: Alternative Fuels and Emissions*. Boca Raton FL: CRC Press, 2010. 3rd ed.
7. Hardalupas Y, Taylor AMKP and Whitelaw JH. Mass flux, mass fraction and concentration of liquid fuel in a swirl-stabilized flame. *Int. J. Multiphase Flow*. 1994; 21: 233–259.
8. Hardalupas Y, Liu CH and Whitelaw JH. Experiments with disk stabilized kerosenefuelled flames. *Combust. Sci. Tech* 1994; 97: 157–191.
9. Masri AR, Dibble RW and Barlow RS. The structure of turbulent nonpremixed flames revealed by Raman-Rayleigh-LIF measurements. *Prog. Energy Combust. Sci* 1996; 22: 307–362.
10. Masri AR, Kalt PAM and Barlow RS. The compositional structure of swirl-stabilised turbulent nonpremixed flames. *Combust. Flame* 2004; 137: 1–37.
11. Masri AR, Kalt PAM, Al-Abdeli YM and Barlow RS. Turbulence–chemistry interactions in non-premixed swirling flames. *Combust. Theory Model* 2007; 11: 653–673.
12. Dally BB, Masri AR, Barlow R.S and Fiechtner G.J. Instantaneous and mean compositional structure of bluff-body stabilized nonpremixed flames. *Combust. Flame* 1998; 114: 119–148.
13. Juddoo M and Masri AR, High-speed OH-PLIF imaging of extinction and re-ignition in non-premixed flames with various levels of oxygenation. *Combust. Flame* 2011; 158: 902–914.
14. Meares S, Prasad VN, Juddoo M, Luo KH and Masri AR. Simultaneous planar and volume cross-LIF imaging to identify out-of-plane motion. *Proc. Combust. Inst* 2015; 35: 3813–3820.
15. Steinberg AM, Boxx I, Arndt CM, Frank JH and Meier W. Experimental study of flame-hole reignition mechanisms in a turbulent non-premixed jet flame using sustained multi-kHz PIV and crossed-plane OH PLIF. *Proc. Combust. Inst* 2011; 33: 1663–1672.
16. Meier W, Duan XR and Weigand P. Investigations of swirl flames in a gas turbine model combustor. *Combust. Flame* 2006; 144: 225–236.
17. Meier W, Boxx I, Stohr M and Carter CD, Laser-based investigations in gas turbine model combustors. *Exp. Fluids* 2010; 49: 865–882.
18. Sutton JA and Driscoll JF. Imaging of local flame extinction due to the interaction of scalar dissipation layers and the stoichiometric contour in turbulent non-premixed flames. *Proc. Combust. Inst* 2007; 31: 1487–1495.
19. Hult J, Meier U, Meier W, Harvey A and Kaminski CF. Experimental analysis of local flame extinction in a turbulent jet diffusion flame by high repetition 2-D laser techniques and multi-scalar measurements. *Proc. Combust. Inst* 2005; 30: 701–709.
20. Böhm B, Heeger C, Boxx I, Meier W and Dreizler A. Time-resolved conditional flow field statistics in extinguishing turbulent opposed jet flames using simultaneous high speed PIV/OH-PLIF. *Proc. Combust. Inst* 2009; 32: 1647–1654.
21. Kaiser SA and Frank JH, Spatial scales of extinction and dissipation in the near field of non-premixed turbulent jet flames. *Proc. Combust. Inst* 2009; 32: 1639–1646.
22. Karpetis AN and Barlow RS. Measurements of scalar dissipation in a turbulent piloted methane/air jet flame. *Proc. Combust. Inst* 2002; 29: 1929–1936.
23. Karpetis AN and Barlow RS, Measurements of flame orientation and scalar dissipation in turbulent partially premixed methane flames. *Proc. Combust. Inst* 2005; 30: 665–672.
24. Barlow RS and Karpetis AN. Measurements of scalar variance, scalar dissipation, and length scales in turbulent piloted methane/air jet flames. *Flow Turbul. Combust* 2004; 72: 427–448.
25. Barlow RS, Frank JH, Karpetis AN and Chen JY. Piloted methane/air jet flames: Transport effects and aspects of scalar structure. *Combust. Flame* 2005; 143: 433–449.
26. Mauss F, Keller D and Peters N. A Lagrangian simulation of flamelet extinction and re-ignition in turbulent jet diffusion flames. *Symp. Combust* 1991; 23: 693–698.
27. Peters N. Local quenching due to flame stretch and non-premixed turbulent combustion. *Combust. Sci. Tech* 1983; 30: 1–17.
28. Peters N. Laminar flamelet concepts in turbulent combustion. *Sym. Combust*. 1986; 21: 1231–1250.
29. Mastorakos E, Taylor AMKP and Whitelaw JH. Scalar dissipation rate at the extinction of turbulent counterflow nonpremixed flames. *Combust. Flame*. 1992; 91: 55–64.
30. Ihme M and Pitsch H. Prediction of extinction and reignition in nonpremixed turbulent flames using a flamelet/progress variable model. *Combust. Flame* 2008; 155: 90–107.
31. Pitsch H, Cha CM and Fedotov S. Flamelet modelling of non-premixed turbulent combustion with local extinction and re-ignition. *Combust. Theory Model* 2003; 7: 317–332.
32. Cha CM, Kosály G and Pitsch H. Modeling extinction and reignition in turbulent nonpremixed combustion using a doubly-conditional moment closure approach. *Phys. Fluids* 2001; 13: 3824.
33. Swaminathan N and Bilger RW. Study of the conditional covariance and variance equations for second order conditional moment closure. *Phys. Fluids* 1999; 11: 2679–2695.
34. Echekki T, Kerstein AR, Dreeben TD and Chen JY. 'One-dimensional turbulence' simulation of turbulent jet diffusion flames: model formulation and illustrative applications. *Combust. Flame* 2001; 125: 1083–1105.
35. Xu J and Pope SB. PDF calculations of turbulent non-premixed flames with local extinction. *Combust. Flame* 2000; 123: 281–307.
36. Lindstedt RP, Louloudi SA and Váos EM. Joint scalar probability density function modeling of pollutant formation in piloted turbulent jet diffusion flames with comprehensive chemistry. *Proc. Combust. Inst* 2000; 28: 149–156.
37. Hewson JC and Kerstein AR. Local extinction and reignition in nonpremixed turbulent CO/H2 /N2 jet flames. *Combust. Sci. Tech*. 2002; 174: 35–66.
38. Prasad VN, Juddoo M, Masri AR, Jones WP and Luo KH. Investigation of extinction and re-ignition in piloted

turbulent non-premixed methane–air flames using LES and high-speed OH-LIF. *Combust. Theory Model* 2013; 17: 483–503.
39. Yuan R, Kariuki J, Dowlut A, Balachandran R and Mastorakos E. Reaction zone visualisation in swirling spray n-heptane flames. *Proc. Combust. Inst* 2015; 35: 1649–1656.
40. Yuan R. *Measurements of Swirl-Stabilised Spray Flames at Blow-off*, PhD thesis, Cambridge University, UK (2015).
41. Masri AR and Gounder JD. Turbulent spray flames of acetone and ethanol approaching extinction. *Combust. Sci. Technol* 2010; 182: 702–715.
42. Zukoski EE and Marble FE. Experiments concerning the mechanism of flame blowoff from bluff bodies. *Guggenheim Jet Propulsion Centre, Report* 1983; 82: 205–10.
43. Yamaguchi S, Ohiwa N and Hasegawa T. Structure and blow-off mechanism of rodstabilized premixed flame. *Combust. Flame* 1985; 62: 31–41.
44. Radhakrishnan K, Heywood JB and Tabaczynski RJ. Premixed turbulent flame blowoff velocity correlation based on coherent structures in turbulent flows. *Combust. Flame* 1981; 42: 19–33.
45. Nair S and Lieuwen T. Acoustic detection of blowout in premixed flames. *J. Propul. Power* 2005; 21: 32–39.
46. Chaudhuri S and Cetegen BM. Blowoff characteristics of bluff-body stabilized conical premixed flames with upstream spatial mixture gradients and velocity oscillations. *Combust. Flame* 2008; 153: 616–633.
47. Chaudhuri S, Kostka S, Renfro MW and Cetegen BM. Blowoff dynamics of bluff body stabilized turbulent premixed flames. *Combust. Flame* 2010; 157: 790–802.
48. Shanbhogue SJ, Husain S and Lieuwen T. Lean blowoff of bluff body stabilized flames: Scaling and dynamics. *Prog. Energy Combust. Sci* 2009; 35: 98–120.
49. Dawson JR, Gordon RL, Kariuki J, Mastorakos E, Masri AR and Juddoo M. Visualization of blow-off events in bluff-body stabilized turbulent premixed flames. *Proc. Combust. Inst* 2011; 33: 1559–1566.
50. Kariuki J, Dawson JR and Mastorakos E. Measurements in turbulent premixed bluff body flames close to blow-off. *Combust. Flame* 2012; 159: 2589–2607.
51. Kariuki J, Dowlut A, Yuan R, Balachandran R and Mastorakos E. Heat release imaging in turbulent premixed methane–air flames close to blow-off. *Proc. Combust. Inst* 2015; 35: 1443–1450.
52. Kalghatgi GT. Blow-out stability of gaseous jet diffusion flames. Part I: in still air. *Combust. Sci. Technol* 1981; 26: 233–239.
53. Broadwell JE, Dahm WJA and Mungal MG. Blowout of turbulent diffusion flames. *Symp. Combust* 1985; 20: 303–310.
54. Dahm WJA and Mayman AG. Blowout limits of turbulent jet diffusion flames for arbitrary source conditions. *AIAA J* 1990; 28: 1157–1162.
55. Stamps D and Tieszen S. Blowout of turbulent jet diffusion flames. *Fuel* 2014; 118: 113–122.
56. Continillo G and Sirignano WA. Counterflow spray combustion modeling. *Combust. Flame* 1990; 81: 325–340.
57. Gutheil E and Sirignano WA. Counterflow spray combustion modeling with detailed transport and detailed chemistry. *Combust. Flame* 1998; 113: 92–105.
58. Gutheil E. Structure and extinction of laminar ethanol-air spray flames. *Combust. Theory Model*. 2001; 5: 131–145.
59. Dvorjetski A and Greenberg JB. Steady-state and extinction analyses of counterflow spray diffusion flames with arbitrary finite evaporation rate. *Combust. Sci. Technol* 2002; 174: 187–208.
60. Mikami M, Miyamoto S and Kojima N, Counterflow diffusion flame with polydisperse sprays. *Proc. Combust. Inst* 2002; 29: 593–599.
61. Moore NJ, McCraw JL and Lyons KM. Observations on jet-flame blowout. *Int. J. React. Syst* 2008; 2008: 1–7.
62. Feikema D, Chen R and Driscoll J. Blowout of nonpremixed flames: maximum coaxial air velocities achievable, with and without swirl. *Combust. Flame* 1991; 86: 347–358.
63. Tyliszczak A, Cavaliere DE and Mastorakos E. LES/CMC of blow-off in a liquid fueled swirl burner. *Flow Turbul. Combust* 2014; 92: 237–267.
64. Marchione T, Ahmed SF and Mastorakos E. Ignition of turbulent swirling n-heptane spray flames using single and multiple sparks. *Combust. Flame* 2009; 156: 166–180.
65. Beér JM and Chigier NA. *Combustion aerodynamics*. New York: Halsted Press Division, Wiley, 1972.
66. Mellor AM. Semi-empirical correlations for gas turbine emissions, ignition, and flame stabilisation. *Prog. Energy Combust. Sci* 1980; 6: 347–358.
67. Mastorakos E, McGuirk JJ and Taylor AMKP. The origin of turbulence acquired by heavy particles in a round, turbulent jet. *Part. Part. Syst. Charact* 1990; 7: 203–208.
68. Hardalupas Y, Taylor AMKP and Whitelaw JH. Velocity and size characteristics of liquid-fuelled flames stabilized by a swirl burner. *Proc. R. Soc. A Math. Phys. Eng. Sci* 990; 428: 129–155.
69. Kourmatzis A, Pham PX and Masri AR. Characterization of atomization and combustion in moderately dense turbulent spray flames. *Combust. Flame* 2015; 162: 978–996.
70. Dumouchel C. On the experimental investigation on primary atomization of liquid streams. *Exp. Fluids* 2008; 45: 371–422.
71. Cavaliere DE. *Blow-off in Gas Turbine Combustors*. PhD thesis, University of Cambridge, UK (2013).
72. Masri AR, Gounder JD, O'Loughlin W, et al. On the boundary conditions and spatial structure of turbulent jet flames of dilute sprays. In: *Seventh Mediterr*. Chia Laguna, Cagliari, Combust. Sym. Sardinia, Italy, 11–15 September, 2011, pp. 1–12.
73. Jones WP and Prasad VN. Large eddy simulation of the Sandia flame series (D–F) using the Eulerian stochastic field method. *Combust. Flame* 2010; 157: 1621–1636.
74. Garmory AE. Capturing localised extinction in Sandia Flame F with LES-CMC. *Combust. Inst* 2011; 33: 1673–1680.
75. Garmory A and Mastorakos E. Sensitivity analysis of LES–CMC predictions of piloted jet flames. *Int. J. Heat Fluid Flow* 2013; 39: 53–63.

Appendix 1

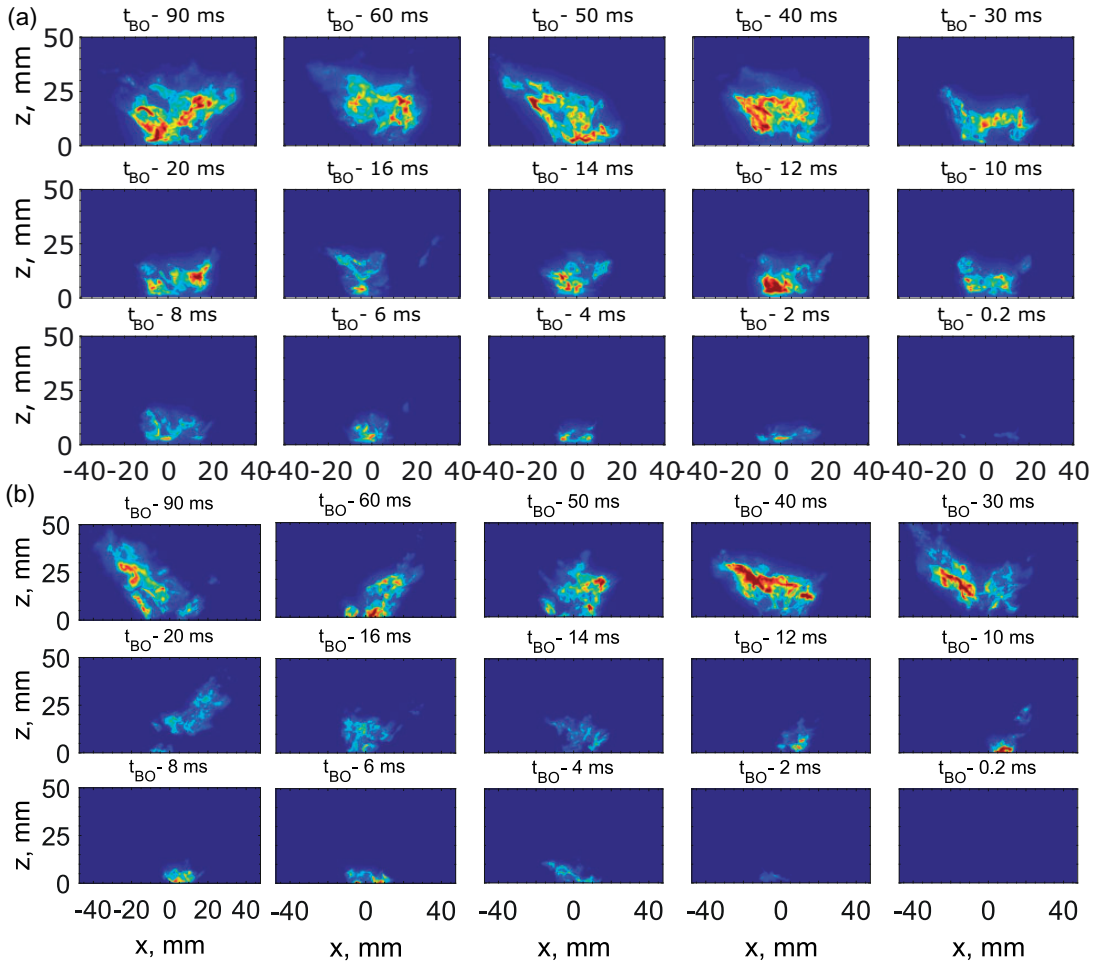

Figure 20. Instantaneous OH* images of swirl-stabilised spray flames of (a) heptane, H1B and (b) dodecane, DD1B, at blow-off transient event (same colour map for each flame). The fuel flow rates of the four flames are the same, at 0.27 g/s. The relative time referenced to the time of complete disappearance of OH* is indicated on top of each image. (a) H1B, $U_B = 22.8$ m/s and (b) DD1B, $U_B = 20.1$ m/s.

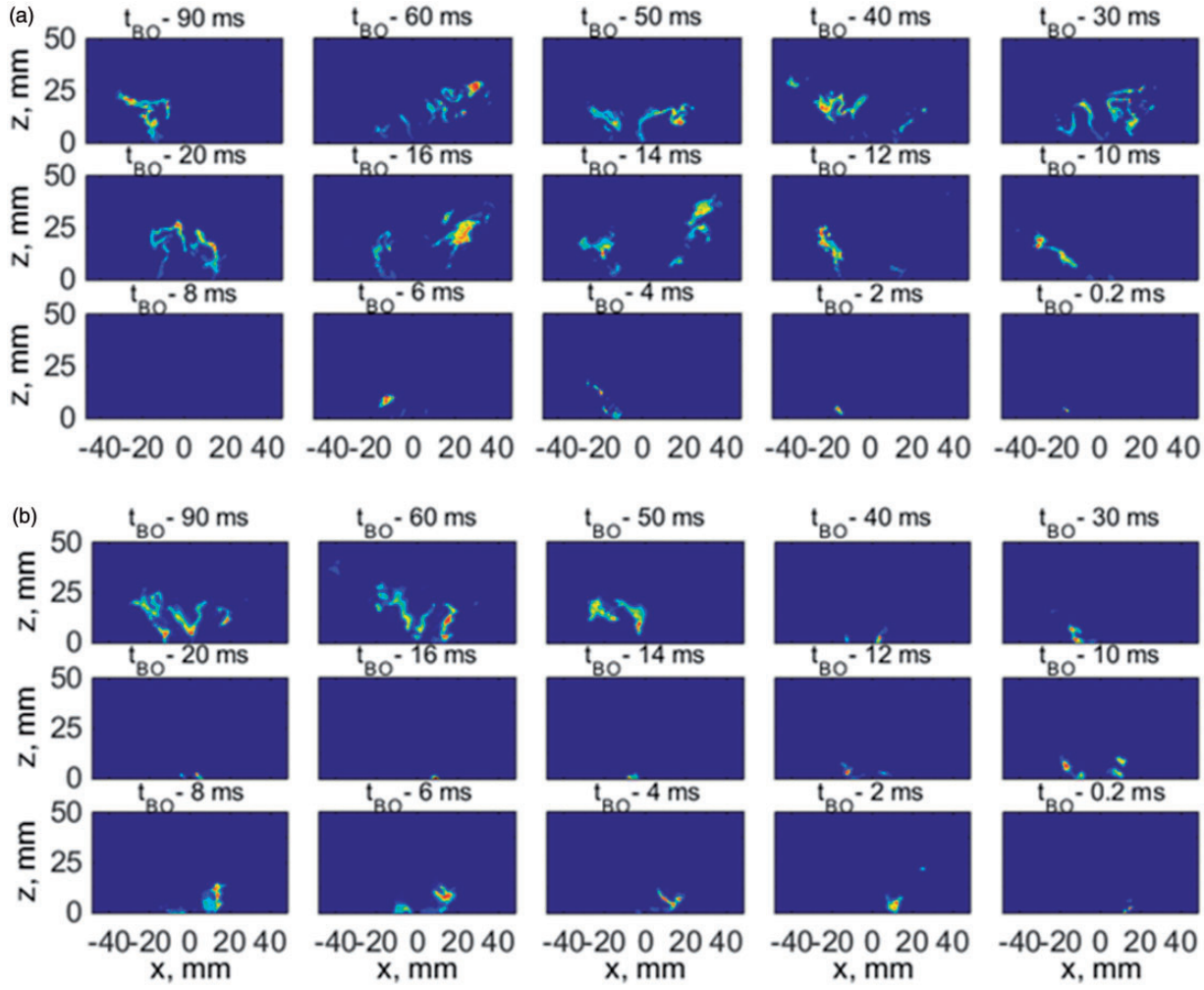

Figure 21. Instantaneous OH-PLIF images from flames of (a) heptane, H1B, and (b) dodecane, DD1B, during the blow-off event (same colour map for each flame). The fuel flow rate was 0.27 g/s and the velocity for each blow-off event is indicated. The relative time referenced to the time of complete disappearance of OH is indicated on top of each image. (a) H1B, $U_B = 22.8$ m/s and (b) DD1B, $U_B = 20.1$ m/s.